UNIVERSIDAD NACIONAL AUTÓNOMA DE MEXICO

DOCTORADO EN CIENCIAS (FÍSICA)

Cooperativity in Matter-Radiation Interaction Models

T E S I S
QUE PARA OPTAR POR EL GRADO DE:

Doctor en Ciencias (Física)

PRESENTA:

LUIS FERNANDO QUEZADA MATA

TUTOR PRINCIPAL

EDUARDO NAHMAD ACHAR
INSTITUTO DE CIENCIAS NUCLEARES

MIEMBROS DEL COMITÉ TUTOR

VÍCTOR MANUEL VELÁZQUEZ AGUILAR
FACULTAD DE CIENCIAS

RAMÓN LÓPEZ PEÑA
INSTITUTO DE CIENCIAS NUCLEARES

Ciudad Universitaria, Cd. Mx., Junio de 2018

Contents

Chapter 1

Introduction

1.1 Abstract

As of today, a vast of human technologies strongly rely on the fundamentals of quantum mechanics, from lasers and transistors (first quantum revolution) to quantum computers and quantum sensors (second quantum revolution). Due to its potential economic implications, there has been an increasing interest to move quantum technologies from the laboratory to the industry, there even is a formal document in Europe (The Quantum Manifesto) to help accomplish this.

The main topic of this thesis lies within the area of cavity quantum electrodynamics (cavity QED), which is the area of physics that studies the interaction of atoms with an electromagnetic field inside an optical cavity. It has been proven to be useful in basic science for elementary verifications of quantum mechanics and in applied science for the development of quantum technologies, specifically on the construction of quantum networks and memories.

This work focuses on the effect that the "cooperation" between atoms has over the quantum phases of systems of two- and three-level atoms interacting with an electromagnetic field. It also examines the behavior of the relevant observables and the entanglement between matter and radiation near the quantum phase transitions. Its main contribution is the explicit definition of the notion of cooperativity for multi-level systems and its application in the analysis of the quantum phases via variational and numerical approaches.

The motivation behind this investigation was the large number of articles that consider fully indistinguishable atoms when dealing with the Hamiltonians here analyzed. The notion of cooperativity allows for the atoms to be treated as semi-distinguishable, an aspect that may be relevant in some experimental realizations of these systems.

In this first chapter I give the motivation and background for my research, citing multiple articles on previous theoretical work, experimental verifications of some aspects of the analyzed models and some of the relevant applications to quantum information theory.

The second chapter covers all the theoretical tools needed to understand the concepts and methodology used in this work. Basic definitions of "quantum phase transitions", "entropy of entanglement" and "fidelity" are included as well as a brief analysis of the studied Hamiltonians. Is in this chapter where I define one of

the central concepts of this thesis, the "cooperation number" for multi-level systems.

The results and its discussion are presented in the third chapter, together with all the graphics obtained from the variational and numerical analysis of some of the observables (energy, population difference between atomic levels and number of photons), fidelity (comparing variational and numerical approaches and between neighboring states) and entropy of entanglement between matter and radiation.

In the forth and last chapter I give some general conclusions of the obtained results and point out the main contributions of this work.

1.2 Background

The interaction between two-level identical atoms and a quantized electromagnetic field, using a dipolar approximation, is described by the Dicke Model [1]. A particularly interesting phenomenon regarding this and other quantum systems are quantum phase transitions (QPT's), which can be thought of as sudden, drastic changes in the physical properties of the ground state of a system at zero temperature due to the variation of some parameter involved in the modeling Hamiltonian. In 1973, Hepp and Lieb [2,3], and Wang and Hioe [4] first theoretically proved the existence of a QPT in the Dicke model. To date, this QPT has been experimentally observed in a Bose-Einstein Condensate coupled to an optical cavity [5,6] and it has been shown to be relevant to quantum information and quantum computing [7,8]. Entanglement between the atoms and the field in the Dicke model has also been studied [9,10], allowing the identification of both quantum and semi-classical, many-body features.

The QPT's of some generalizations of the Dicke model, which consider atoms of three or more levels, have also been extensively studied [13,27–35]. These models allow meaningful interactions with two or more modes of the electromagnetic field, a feature that has been exploited for the development of certain types of quantum memories [37–40].

An important aspect of these matter-radiation interaction models is the distinguishability of the atoms, a characteristic that depends on the space we choose for the Hamiltonian to act on. Most works on the subject treat the atoms as completely indistinguishable, as they only consider Fock-like (number) states to describe them; this, however, may not correctly describe some of the experimental realizations of the models. To gain distinguishability we must add information of the atomic field to the states we use to describe it, this information is the *cooperation number*, a quantity closely related to the group's representation of the atomic field.

The term "cooperation number" was first introduced by Dicke in his original paper [1], referring to the different representations of SU(2) used in the description of the full state's space of his Hamiltonian, and whose physical interpretation is that of an effective number of atoms in the system, i.e., the number of atoms that contribute to the energy of the atomic field.

In this work, in order to study the influence of the cooperation number over the QPT's, we use a variational approach to estimate the ground state of a system of a finite number of two- and three-level atoms respectively interacting in a dipolar approximation with a two- and a one-mode electromagnetic field. We analyze the influence of the cooperation number over the QPT's via the expectation values of the relevant observables of

the system and the entropy of entanglement between matter and radiation.

For three-level systems, realized as spin-1 particles, the entropy of entanglement has been studied by writing their density matrices in the spin tomographic probability representation. The von Neumann entropy of the qutrit state is then shown to satisfy the entropic inequality, which is the subadditivity condition analogous to the subadditivity condition for bipartite systems of two qubits [45]. It is interesting to note that the information and entropic relations, which are known for classical probability distributions, are also valid for quantum system states described by the tomographic probability distributions [46]. This approach, however, has not considered cooperation numbers nor has it been used in connection to QPT.

Chapter 2

Theoretical Framework

2.1 Fidelity (F)

Fidelity is a measure of the similarity between two quantum states; given $|\phi\rangle$ and $|\varphi\rangle$ it is defined as

$$F(|\phi\rangle, |\varphi\rangle) := |\langle\phi|\varphi\rangle|^2 . \tag{2.1}$$

This definition of fidelity is the one we will be using to compare our variational solutions to numerical ones.

On the other hand, across a QPT the ground state of a system suffers a sudden, drastic change, thus it is natural to expect a drop in the fidelity between neighboring states near the transition:

$$F(|\psi\rangle, \mu) := |\langle\psi(\mu)|\psi(\mu+\delta)\rangle|^2 , \tag{2.2}$$

where $\delta \ll 1$. This drop has been, in fact, already shown to happen for two and three-level systems [11, 15, 25] for fully indistinguishable atoms, and is the one we will be using to characterize the QPT's of our systems.

2.2 Quantum Phase Transitions

The formal definition of the concept of "quantum phase" is that of an open region $\mathcal{R} \subseteq \mathbb{R}^\ell$ where the ground state's energy $\mathcal{E}_0$, as a function of ℓ parameters involved in the modeling Hamiltonian, is analytic. Thus a QPT is identified by the boundary $\partial\mathcal{R}$ of the region at which $\frac{\partial^n \mathcal{E}_0}{\partial x^n}$ is discontinuous for some n (known as the order of the transition).

Notice that in the previous definition, for the sake of generality, we did not consider the thermodynamic limit, as it has been shown that interesting phenomena regarding QPT's occur even for a finite number of particles [11, 12].

The description of quantum phase that we will be using throughout this work is that of an open region in the space of parameters where the fidelity between neighboring states is close to 1, therefore the QPT's will be characterized by drops in the value of this fidelity.

2.3 Entropy of entanglement (S_ε)

Entropy of entanglement is defined for a bipartite system as the von Neumann entropy of either of its reduced states, that is, if ρ is the density matrix of a system in a Hilbert space $\mathcal{H} = \mathcal{H}_1 \otimes \mathcal{H}_2$, its entropy of entanglement is defined as

$$S_\varepsilon := -Tr\left\{\rho_1 \log \rho_1\right\} = -Tr\left\{\rho_2 \log \rho_2\right\}, \tag{2.3}$$

where $\rho_1 = Tr_2\left\{\rho\right\}$ and $\rho_2 = Tr_1\left\{\rho\right\}$.

The Hamiltonians we will consider model a bipartite system formed by matter and radiation subsystems, which means that their entropy of entanglement can be used to see the influence of the cooperation number and the QPT over its behavior.

2.4 Two-level Atoms

2.4.1 Modeling Hamiltonian

The Hamiltonian (Dicke's Hamiltonian) describing the interaction, in a dipolar approximation, between N two-level identical atoms (same energy difference between the two levels) and one-mode of an electromagnetic field in an ideal cavity, has the expression ($\hbar = 1$)

$$H_D = \omega_A J_z + \Omega a^\dagger a - \frac{\gamma}{\sqrt{N}}\left(J_- + J_+\right)\left(a + a^\dagger\right). \tag{2.4}$$

Here, ω_A is the energy difference between the atomic levels, Ω is the frequency of the field's mode, γ is the dipolar coupling constant, J_z, J_-, J_+ are the collective spin operators and a, $a^\dagger$ are the annihilation and creation operators for the electromagnetic field. The multi-mode Hamiltonian is obtained summing over the number k of modes [13], and has the expression

$$H = \omega_A J_z + \sum_{\imath=1}^{k} \Omega_\imath a_\imath^\dagger a_\imath - \frac{1}{\sqrt{N}} \sum_{\imath=1}^{k} \gamma_\imath \left(J_- + J_+\right)\left(a_\imath + a_\imath^\dagger\right). \tag{2.5}$$

The k modes of the electromagnetic field are described in terms of annihilation and creation operators for each mode $a_\imath$, $a_\imath^\dagger$, acting on the tensor product of k copies of the Fock space $\bigotimes_{\imath=1}^{k} \mathcal{F}_\imath$ and satisfying the commutation relations

$$\left[a_\imath, a_\jmath^\dagger\right] = \delta_{\imath\jmath}, \qquad \left[a_\imath, a_\jmath\right] = \left[a_\imath^\dagger, a_\jmath^\dagger\right] = 0. \tag{2.6}$$

A two-level atom is described using the $\frac{1}{2}$-spin matrices $S_z = \frac{1}{2}\sigma_z$, $S_\pm = \frac{1}{2}\left(\sigma_x \pm i\sigma_y\right)$ (σ_x, σ_y and σ_z being the Pauli matrices), which act on a two-dimensional complex Hilbert space $\mathbb{C}^2$ and satisfy the commutation relations

$$\left[S_+, S_-\right] = 2S_z, \qquad \left[S_z, S_\pm\right] = \pm S_\pm. \tag{2.7}$$

When considering a system of N two-level atoms, we use the collective spin operators J_z, J_-, J_+ defined as

$$J_\diamond = S_\diamond \otimes I_2^{\otimes(N-1)} + I_2 \otimes S_\diamond \otimes I_2^{\otimes(N-2)} + \cdots + I_2^{\otimes(N-2)} \otimes S_\diamond \otimes I_2 + I_2^{\otimes(N-1)} \otimes S_\diamond \tag{2.8}$$

where I_2 is the identity operator on $\mathbb{C}^2$ and $\diamond \in \{z, -, +\}$. These collective spin operators satisfy the commutation relations

$$[J_+, J_-] = 2J_z, \qquad [J_z, J_\pm] = \pm J_\pm \tag{2.9}$$

and act, in principle, on the complex Hilbert space $\left(\mathbb{C}^2\right)^{\otimes N}$; however, working with this space is physically equivalent to studying a system of N fully distinguishable atoms, which we don't usually have in the experimental setups used in the study of the QPT in the Dicke model. To overcome this issue, we must use the common set of eigenvectors $\{|j,m\rangle\}$ of the two commuting observables J_z and $J^2 = \frac{1}{2}\left(J_+J_- + J_-J_+\right) + J_z^2$, where the label j is limited to the values $j \in \left\{r, r+1, \ldots, \frac{N}{2}\right\}$ ($r = 0$ for even N and $r = \frac{1}{2}$ for odd N) and the label $m \in \mathbb{Z}$ is constricted by $|m| \leq j$. These vectors do not form a basis of $\left(\mathbb{C}^2\right)^{\otimes N}$ for $N > 2$, as the dimension of their linear span is

$$\dim\left\{\text{span}\left\{\{|j,m\rangle\}_{|m|\leq j}^{j=r,\ldots,\frac{N}{2}}\right\}\right\} = \sum_{j=r}^{\frac{N}{2}} (2j+1) \leq 2^N.$$

We will denote by $\mathcal{H}_A$ the subspace of $\left(\mathbb{C}^2\right)^{\otimes N}$ generated by the states $\{|j,m\rangle\}_{|m|\leq j}^{j=r,\ldots,\frac{N}{2}}$.

There are two main results concerning the states $\{|j,m\rangle\}_{|m|\leq j}^{j=r,\ldots,\frac{N}{2}}$ and the space $\mathcal{H}_A$: the first comes from noticing that $\left[H, J^2\right] = 0$, which means that the label j of the eigenvalues of J^2 remains constant during the system's evolution; the second is the decomposition $\mathcal{H}_A = \bigoplus_{j=r}^{\frac{N}{2}} \mathcal{H}_j$, where each $\mathcal{H}_j$ is the subspace of dimension $\dim\{\mathcal{H}_j\} = 2j+1$ generated by the states $\{|j,m\rangle\}_{|m|\leq j}$ with a fixed j. In this treatment, in order to study indistinguishable atoms, we are ignoring the multiplicities $g(j)$ of the irreducible representations of $SU(2)$, i.e. the number of times that each $\mathcal{H}_j$ appears in the full decomposition $\left(\mathbb{C}^2\right)^{\otimes N} = \bigoplus_{j=r}^{\frac{N}{2}} g(j)\,\mathcal{H}_j$.

To make it clear that the space $\mathcal{H}_A$ is the one we must work with when indistinguishable atoms are considered we should inquire into the physical interpretation of the labels j and m. In order to give a physical interpretation to the label j we must notice that the energy of the atomic system is bounded by $\pm j\omega$ independently of the number of atoms N (but with the restriction $j \leq \frac{N}{2}$), this leads us to interpret the quantity $2j$ as the effective number of atoms in the system and define it as the cooperation number (for two-level atoms). To make the notion of the cooperation number more intuitive, Dicke, in his original paper [1], compares a state with $j = 0$, which exists only for an even number of atoms, with a classical system of an even number of oscillators swinging in pairs oppositely phased. The interpretation of the label m is clear from the definition of J_z: $m = \frac{1}{2}(n_e - n_g)$, where n_e and n_g are the number of atoms in the excited and ground states, respectively.

In this work we restrict our analysis to the space $\mathcal{H}_A$, as it allows us to choose j as an initial condition (which will remain constant) and work in $\mathcal{H}_j$, where $2j$ atoms are indistinguishable.

2.4.2 Methodology

There have been various contributions to the study of the phase transition in the Dicke model (and other two-level models) [14–18] and different approaches such as Husimi function analysis [19], entropic uncertainty relations [20] and energy surface minimization [21–26], have been used for its investigation.

In this work we use the energy surface minimization method, which consists on minimizing the surface that is obtained by taking the expectation value of the modeling Hamiltonian with respect to some trial variational state. The strength of this method lies on the choice of the trial state, as it is the latter, after minimization, the one that will be modeling the ground state of the system.

Here we take a variational approach for both matter and radiation fields, and show how to calculate the QPT of the system modeled by Hamiltonian 2.5 via four means:

1. Using a tensor product of Heisenberg-Weyl HW(1) coherent states for each mode of the electromagnetic field and SU(2) coherent states for the atomic field as trial states, and analytically minimizing the obtained energy surface with respect to its parameters.

2. Using a projection operator on HW(1) coherent states and SU(2) coherent states to obtain trial states that preserve the parity symmetry of the Hamiltonian with respect to the total excitation number of the system (*symmetry adapted states*), and numerically minimize the obtained energy surface with respect to its parameters.

3. Using symmetry adapted states, as in (2) above, to obtain the energy surface and "minimize" it with the minimizing parameters obtained in (1) above, thus allowing us to have analytic expressions for the ground state.

4. Numerically diagonalizing the Hamiltonian, which gives us the exact quantum solution.

2.4.2.1 Coherent States (CS)

For each mode of the electromagnetic field the annihilation and creation operators $a_\imath$ and $a_\imath^\dagger$, appearing in the modeling Hamiltonian 2.5, satisfy the commutation relations (2.6) of the Lie algebra generators of the Heisenberg-Weyl group HW(1); hence, a natural choice of a trial state for the radiation field is a tensor product of k (number of modes) coherent states of HW(1)

$$|\bar{\alpha}\rangle := |\alpha_1\rangle \otimes \cdots \otimes |\alpha_k\rangle \,, \tag{2.10}$$

where each $|\alpha_\imath\rangle$ is defined as

$$|\alpha_\imath\rangle := e^{\alpha_\imath a_\imath^\dagger - \alpha_\imath^* a_\imath} |0_\imath\rangle = e^{-\frac{|\alpha_\imath|^2}{2}} \sum_{\nu_\imath=0}^{\infty} \frac{\alpha_\imath^{\nu_\imath}}{\sqrt{\nu_\imath!}} |\nu_\imath\rangle \,. \tag{2.11}$$

Furthermore, the commutation relations of the collective spin operators J_-, J_+ and J_z (2.9) are the same as the ones of the Lie algebra generators of the special unitary group SU(2). Thus, analogously as for the radiation field, we use the coherent states of SU(2)

$$|\xi\rangle_j := \left|\frac{\upsilon \tan|\upsilon|}{|\upsilon|}\right\rangle_j := e^{\upsilon J_+ - \upsilon^* J_-}\,|j,0\rangle = \frac{1}{\left(1+|\xi|^2\right)^j}\sum_{m=0}^{2j}\binom{2j}{m}^{\frac{1}{2}}\xi^m\,|j,m-j\rangle\,. \tag{2.12}$$

as trial states for the matter field.

2.4.2.2 Symmetry Adapted States (SAS)

The modeling Hamiltonian we are considering has a parity symmetry given by $\left[e^{i\pi\Lambda}, H\right] = 0$, where $\Lambda = \sqrt{J^2+\frac{1}{4}} - \frac{1}{2} + J_z + \sum_{\imath=1}^{k} a_\imath^\dagger a_\imath$ is the excitation number operator with eigenvalues $\lambda = j + m + \sum_{\imath=1}^{k}\nu_\imath$. This symmetry allows us to classify its eigenstates in terms of the parity of the eigenvalues λ; however, as states with opposite symmetry are strongly mixed by the CS defined in the previous section, we should then adapt this symmetry to the CS by projecting them with the operator $P_\pm = \frac{1}{2}\left(I \pm e^{i\pi\Lambda}\right)$, i.e.

$$|\bar{\alpha},\xi_j\rangle_\pm := \mathcal{N}_\pm P_\pm\,|\bar{\alpha}\rangle\otimes|\xi\rangle_j = \mathcal{N}_\pm\left(|\bar{\alpha}\rangle\otimes|\xi\rangle_j \pm |-\bar{\alpha}\rangle\otimes|-\xi\rangle_j\right), \tag{2.13}$$

with $\mathcal{N}_\pm = \left(2 \pm 2E\,(-\cos\theta)^{2j}\right)^{-\frac{1}{2}}$ the normalization factors for the even (+) and odd (-) states (where $E = \exp\left\{-2\sum_{\imath=1}^{k}\left|\alpha_\imath^2\right|\right\}$ and we have written $\xi = \tan\left(\frac{\theta}{2}\right)e^{i\phi}$).

As we are interested in the ground state of the system, which has an even parity, we only focus on the state $|\bar{\alpha},\xi_j\rangle_+$.

2.5 Three-level Atoms

2.5.1 Modeling Hamiltonian

The Hamiltonian describing the interaction, in a dipolar approximation, between N three-level identical atoms (same energy levels) and one-mode of an electromagnetic field in an ideal cavity, has the expression ($\hbar = 1$) [13]

$$H = \overline{\omega}_1 e_{11} + \overline{\omega}_2 e_{22} + \overline{\omega}_3 e_{33} + \Omega a^\dagger a - \frac{1}{\sqrt{N}}\sum_{i<j}^{3}\mu_{ij}\left(e_{ij} + e_{ij}^\dagger\right)\left(a + a^\dagger\right). \tag{2.14}$$

Here, $\overline{\omega}_1$, $\overline{\omega}_2$ and $\overline{\omega}_3$ are the three energy levels of the atoms, with $\overline{\omega}_1 \le \overline{\omega}_2 \le \overline{\omega}_3$, Ω is the frequency of the field's mode, μ_{ij} are the dipolar coupling parameters between the radiation and the pair of atomic levels i and j, a and $a^\dagger$ are the annihilation and creation operators for the electromagnetic field, and e_{ij} are the collective atomic matrices (annihilation operators for the atomic field), i.e., summations with as many summands as atoms in the system (as in equation 2.8), of the single-entry matrices $(\bar{e}_{ij})_{mn} = \delta_{im}\delta_{jn}$. Choosing the zero of the energy to be at $\frac{1}{3}\left(\overline{\omega}_1 + \overline{\omega}_2 + \overline{\omega}_3\right)$ we can rewrite Hamiltonian 2.14 in the more useful form

$$H = \omega_1 J_z^{(1)} + \omega_2 J_z^{(2)} + \Omega a^\dagger a - \frac{1}{\sqrt{N}}\sum_{i<j}^{3}\mu_{ij}\left(e_{ij} + e_{ij}^\dagger\right)\left(a + a^\dagger\right), \tag{2.15}$$

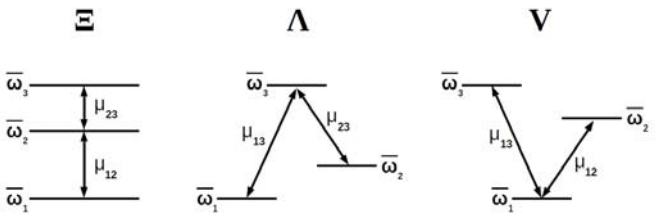

Figure 2.1: Diagram showing the three possible configurations of a three-level atom according to the permitted transitions between its levels.

where $J_z^{(1)} = \frac{1}{2}(e_{22} - e_{11})$ (half the population difference between the second and first levels), $J_z^{(2)} = \frac{1}{2}(e_{33} - e_{22})$ (half the population difference between the third and second levels), $\omega_1 = -\frac{4}{3}\overline{\omega}_1 + \frac{2}{3}\overline{\omega}_2 + \frac{2}{3}\overline{\omega}_3$ and $\omega_2 = -\frac{2}{3}\overline{\omega}_1 - \frac{2}{3}\overline{\omega}_2 + \frac{4}{3}\overline{\omega}_3$.

Selection rules for a dipolar transition force the parity of the quantum states between which the transition is made to be opposite, and hence to one of the coupling parameters μ_{ij} to be zero, giving rise to three possible three-level atom configurations: Ξ configuration ($\mu_{13} = 0$), Λ configuration ($\mu_{12} = 0$) and V configuration ($\mu_{23} = 0$) (Figure 2.1).

2.5.2 Representation Theory and Cooperation number

The term cooperation number was first introduced by Dicke in his original paper [1], referring to the different representations of $SU(2)$ used in the description of the full state's space of his Hamiltonian. Here we make a brief analysis of the representations of $SU(3)$ and its basis states (Gelfand-Tsetlin states), which we later use to describe the three-level atoms in our system.

The operators $J_z^{(1)}$, $J_z^{(2)}$, e_{12}, e_{23}, e_{13}, $e_{12}^\dagger$, $e_{23}^\dagger$ and $e_{13}^\dagger$ in Hamiltonian (2.15), form a basis for the Lie algebra of $SU(3)$, one that is particularly convenient if it is adopted along with the labeling scheme devised by Gelfand and Tsetlin [41] for the basis states of the irreducible representations (irreps) of $SU(n)$. Given an irrep $h = (h_1, h_2, h_3)$ of $SU(3)$, the scheme, called a Gelfand-Tsetlin pattern, is as follows:

$$\left| \begin{array}{ccc} h_1 & h_2 & h_3 \\ q_1 & q_2 & \\ r & & \end{array} \right\rangle$$

where the top row contains the information that specifies the irrep, while the entries of lower rows are subject to the betweenness conditions: $h_1 \geq q_1 \geq h_2$, $h_2 \geq q_2 \geq h_3$ and $q_1 \geq r \geq q_2$.

These basis states are simultaneous eigenstates of the operators $J_z^{(1)}$ and $J_z^{(2)}$:

$$J_z^{(1)} \left| \begin{array}{ccc} h_1 & h_2 & h_3 \\ q_1 & q_2 & \\ r & & \end{array} \right\rangle = \left(\frac{1}{2}(q_1 + q_2) - r\right) \left| \begin{array}{ccc} h_1 & h_2 & h_3 \\ q_1 & q_2 & \\ r & & \end{array} \right\rangle \tag{2.16a}$$

$$J_z^{(2)} \left| \begin{array}{ccc} h_1 & h_2 & h_3 \\ q_1 & q_2 & \\ r & & \end{array} \right\rangle = \left(\frac{1}{2}(h_1 + h_2 + h_3 + r) - (q_1 + q_2)\right) \left| \begin{array}{ccc} h_1 & h_2 & h_3 \\ q_1 & q_2 & \\ r & & \end{array} \right\rangle, \tag{2.16b}$$

explicit formulas exist for the matrix elements of e_{12}, e_{23}, $e_{12}^\dagger$ and $e_{23}^\dagger$ [42]:

$$e_{12}\left|\begin{array}{ccc} h_1 & h_2 & h_3 \\ q_1 & q_2 & \\ r & & \end{array}\right\rangle = \sqrt{(q_1 - r)\,(r - q_2 + 1)}\left|\begin{array}{ccc} h_1 & h_2 & h_3 \\ q_1 & q_2 & \\ r+1 & & \end{array}\right\rangle \tag{2.17a}$$

$$\begin{aligned} e_{23}\left|\begin{array}{ccc} h_1 & h_2 & h_3 \\ q_1 & q_2 & \\ r & & \end{array}\right\rangle &= \sqrt{\frac{(h_1 - q_2 + 1)\,(h_2 - q_2)\,(q_2 - h_3 + 1)\,(r - q_2)}{(q_1 - q_2 + 1)\,(q_1 - q_2)}}\left|\begin{array}{ccc} h_1 & h_2 & h_3 \\ q_1 & q_2 + 1 & \\ r & & \end{array}\right\rangle \\ &+ \sqrt{\frac{(h_1 - q_1)\,(h_2 - q_1 - 1)\,(h_3 - q_1 - 2)\,(q_1 - r + 1)}{(q_2 - q_1 - 1)\,(q_2 - q_1 - 2)}}\left|\begin{array}{ccc} h_1 & h_2 & h_3 \\ q_1 + 1 & q_2 & \\ r & & \end{array}\right\rangle \end{aligned} \tag{2.17b}$$

$$e_{12}^\dagger\left|\begin{array}{ccc} h_1 & h_2 & h_3 \\ q_1 & q_2 & \\ r & & \end{array}\right\rangle = \sqrt{(r - q_2)\,(q_1 - r + 1)}\left|\begin{array}{ccc} h_1 & h_2 & h_3 \\ q_1 & q_2 & \\ r-1 & & \end{array}\right\rangle \tag{2.17c}$$

$$\begin{aligned} e_{23}^\dagger\left|\begin{array}{ccc} h_1 & h_2 & h_3 \\ q_1 & q_2 & \\ r & & \end{array}\right\rangle &= \sqrt{\frac{(h_1 - q_2 + 2)\,(h_2 - q_2 + 1)\,(q_2 - h_3)\,(r - q_2 + 1)}{(q_1 - q_2 + 2)\,(q_1 - q_2 + 1)}}\left|\begin{array}{ccc} h_1 & h_2 & h_3 \\ q_1 & q_2 - 1 & \\ r & & \end{array}\right\rangle \\ &+ \sqrt{\frac{(h_1 - q_1 + 1)\,(h_2 - q_1)\,(h_3 - q_1 - 1)\,(q_1 - r)}{(q_2 - q_1)\,(q_2 - q_1 - 1)}}\left|\begin{array}{ccc} h_1 & h_2 & h_3 \\ q_1 - 1 & q_2 & \\ r & & \end{array}\right\rangle \end{aligned} \tag{2.17d}$$

and they allow us to have a very simple physical interpretation of its parameters in our particular context: r is the number of atoms in the first (lowest) energy level, $q_1 + q_2 - r$ is equal to the number of atoms in the second energy level and $h_1 + h_2 + h_3 - q_1 - q_2$ is equal to the number of atoms in the third (highest) energy level, where h_1, h_2 and h_3 are subject to the constraint $h_1 + h_2 + h_3 = N$ (the total number of atoms).

The operators of the atomic subsystem in Hamiltonian 2.15 act, in principle, on the complex Hilbert space $\left(\mathbb{C}^3\right)^{\otimes N}$, which has a dimension of 3^N; this space can be decomposed into a direct sum of subspaces $\mathcal{H}_h$ labeled by the permitted representations h of $SU(3)$ for a given N:

$$\left(\mathbb{C}^3\right)^{\otimes N} = \bigoplus_h g_h \mathcal{H}_h,$$

where g_h is the representation's multiplicity (the number of times the representation appears in the decomposition) and the sum runs over all possible representations $h = (h_1, h_2, h_3)$ such that $h_1 + h_2 + h_3 = N$ and $h_1 \geq h_2 \geq h_3$ (from the betweenness condition of the Gelfand-Tsetlin patterns). Nevertheless, working with this space is physically equivalent to studying a system of N fully distinguishable atoms, which we don't usually have in experimental realizations of the studied system. If we were to consider every possible represen-

tation with its own multiplicity, we would be treating the atoms as fully distinguishable; on the other hand, if we just consider the symmetric representation ($h_1 = N$, $h_2 = h_3 = 0$), we would be treating the atoms as fully indistinguishable. Here we consider every possible representation but ignore its multiplicity, leading us to treat the atoms as semi-distinguishable, the cooperation number being what adds some distinguishability to the states.

The idea behind the term "cooperation number", as described by Dicke, is that of an effective number of atoms in the system, however this notion by itself is hard to generalize to n-level systems without a proper definition. Here we define the cooperation number (n_c) to be the maximum difference in the number of atoms between any pair of levels. This number changes depending on the representation of $SU(n)$ we use to describe the system: for an arbitrary representation $h = (h_1, h_2, \ldots, h_n)$ the cooperation number is found to be

$$n_c = h_1 - h_n. \tag{2.18}$$

In this particular section, where three-level atoms are being studied, the cooperation number (2.18) is simply $n_c = h_1 - h_3$. Notice that a state with $n_c = 0$ will have an expectation value of 0 for the energy operator (2.15).

Notice that this definition is consistent when two-level atoms are considered, as the states $|j, m\rangle$ written in the Gelfand-Tsetlin labeling scheme are

$$\left| \begin{array}{cc} \frac{N}{2}+j & \frac{N}{2}-j \\ \frac{N}{2}-m & \end{array} \right\rangle$$

It is worth mentioning that the parameters h_1, h_2 and h_3 are functions which depend on the total number of atoms (a constant) and the eigenvalues of the Casimir operators of $SU(3)$ (which, by definition, commute with the atomic operators and therefore with Hamiltonian 2.15), this means that the representation parameters and hence the cooperation number are constants of motion in the studied model.

2.6 Methodology

To study the QPT's in our system we need to know its ground state; in this work we use a variational approach and apply the energy surface minimization method to estimate it. This method consists on minimizing the surface that is obtained by taking the expectation value of the modeling Hamiltonian with respect to some trial variational state. The minimization is taken with respect to all the field and matter parameters (see below). The strength of this method lies on the choice of the trial state, as it is the latter, after minimization, the one that will be modeling the ground state of the system.

Here we take a variational approach for both the matter and the radiation field, using a tensor product of $HW(1)$ coherent states for the radiation field, and $SU(3)$ coherent states for the atomic field. Note that, since we are using a tensor product of field and matter states as our trial state, it will not account for entanglement between the two subsystems.

As our system is not integrable, and the expression for the energy surface is unwieldy, the minimization is carried out numerically.

2.6.1 Coherent States of $SU(3)$

For the atomic field, as we have already mentioned, the operators $J_z^{(1)}$, $J_z^{(2)}$, e_{12}, e_{23}, e_{13}, $e_{12}^\dagger$, $e_{23}^\dagger$ and $e_{13}^\dagger$ form a basis for the Lie algebra of $SU(3)$, thus it is natural to use the coherent states of $SU(3)$ as trial states; these are defined as the application of the exponentials of the raising operators $e_{12}^\dagger$, $e_{23}^\dagger$ and $e_{13}^\dagger = \left[e_{23}^\dagger, e_{12}^\dagger\right]$ to the atomic lowest energy state, and in the Gelfand-Tsetlin scheme take the form:

$$|\gamma, h\} := e^{\gamma_3 e_{12}^\dagger} e^{\gamma_2 e_{13}^\dagger} e^{\gamma_1 e_{23}^\dagger} \left| \begin{array}{ccc} h_1 & h_2 & h_3 \\ h_1 & h_2 & \\ h_1 & & \end{array} \right\rangle,$$

where the delimiters $|\cdot\}$ mean the state is not normalized. Performing this calculation gives us the following expression for the coherent states of $SU(3)$:

$$\begin{aligned} |\gamma, h\} = \sum_{n=0}^{h_2-h_3} \sum_{\ell=0}^{h_1-h_2} \sum_{m=0}^{h_2-h_3-n} \sum_{j=0}^{h_1-h_2-\ell+n} & \gamma_1^n \gamma_2^{\ell+m} \gamma_3^j \\ & \cdot \begin{pmatrix} h_2-h_3 \\ n \end{pmatrix}^{\frac{1}{2}} \begin{pmatrix} h_1-h_2-\ell+n \\ j \end{pmatrix}^{\frac{1}{2}} \begin{pmatrix} m+j \\ j \end{pmatrix}^{\frac{1}{2}} \\ & \cdot \frac{S_{\ell m n}(h)}{(\ell+m)!} \left| \begin{array}{ccc} h_1 & h_2 & h_3 \\ h_1-\ell & h_2-n-m & \\ h_1-\ell-m-j & & \end{array} \right\rangle. \end{aligned} \tag{2.19}$$

Here, the numbers $S_{\ell m n}(h)$ are defined as the scalars obtained from the application of the operator $\left(e_{13}^\dagger\right)^{\ell+m}$ to the resulting states from the previous application of $e^{\gamma_1 e_{23}^\dagger}$, namely:

$$\left(e_{13}^\dagger\right)^{\ell+m} \left| \begin{array}{ccc} h_1 & h_2 & h_3 \\ h_1 & h_2-n & \\ h_1 & & \end{array} \right\rangle = S_{\ell m n}(h) \left| \begin{array}{ccc} h_1 & h_2 & h_3 \\ h_1-\ell & h_2-n-m & \\ h_1-\ell-m & & \end{array} \right\rangle \tag{2.20}$$

In order to obtain the ground state of the system we minimize the expectation value of the Hamiltonian (energy surface) with respect to the real and imaginary parts of the field parameter α and the matter parameters γ_i, $(i = 1, 2, 3)$.

Chapter 3

Results and Discussion

3.1 Two-level Atoms

Writing the complex labels $\alpha_\imath$ and ξ as $\alpha_\imath = q_\imath + ip_\imath$ and $\xi = \tan\left(\frac{\theta}{2}\right) e^{i\phi}$, with $q_\imath, p_\imath \in \mathbb{R}$, $\theta \in [0, \pi)$, $\phi \in [0, 2\pi)$, the CS's energy surface is obtained by taking the expectation value of Hamiltonian 2.5 with respect to the state $|\bar{\alpha}\rangle \otimes |\xi\rangle_j$, and has the form

$$\mathcal{H}_{j,CS}\left(q_\imath, p_\imath, \theta, \phi\right) := \langle\bar{\alpha}| \otimes \langle\xi|_j H |\bar{\alpha}\rangle \otimes |\xi\rangle_j = -j\omega_A \cos\theta + \sum_{\imath=1}^{k} \Omega_\imath \left(q_\imath^2 + p_\imath^2\right) - \frac{4j}{\sqrt{N}} \sin\theta \cos\phi \sum_{\imath=1}^{k} \gamma_\imath q_\imath. \quad (3.1)$$

The critical points which minimize it are then found to be

$$\theta_c = q_{\imath_c} = p_{\imath_c} = 0, \qquad \text{for } \omega_A \geq \frac{8j}{N} \sum_{\imath=1}^{k} \frac{\gamma_\imath^2}{\Omega_\imath},$$

$$\left.\begin{array}{l} \cos\theta_c = \frac{N\omega_A}{8j} \left(\sum_{\imath=1}^{k} \frac{\gamma_\imath^2}{\Omega_\imath}\right)^{-1}, \\ \phi_c = 0, \pi, \\ q_{\imath_c} = \frac{2j\gamma_\imath}{\Omega_\imath \sqrt{N}} \cos\phi_c \sin\theta_c, \\ p_{\imath_c} = 0 \end{array}\right\} \quad \text{for } \omega_A < \frac{8j}{N} \sum_{\imath=1}^{k} \frac{\gamma_\imath^2}{\Omega_\imath}.$$

Substituting these values into (3.1) we obtain the energy of the coherent ground state as a function of the Hamiltonian parameters,

$$\mathcal{E}_{CS}\left(\omega_A, \gamma_\imath\right) = \begin{cases} -j\omega_A & , \quad \text{for } \delta \geq 1 \\ -\frac{j\omega_A}{2}\left(\frac{1}{\delta} + \delta\right) & , \quad \text{for } \delta < 1, \end{cases} \quad (3.2)$$

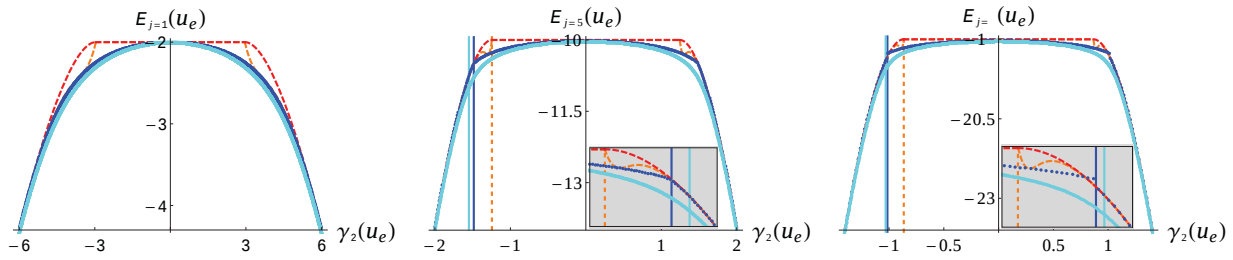

Figure 3.1: Energy of the ground state as a function of γ_2 obtained using CS (red), SAS with CS's minima (orange), SAS minimized numerically (blue) and quantum solution (cyan). Vertical lines show the transition according to the quantum solution via fidelity's minimum (cyan), SAS minimized numerically (dark gray / blue online) and SAS with CS's minima (orange). Left: j=1, center: j=5, right: j=9. Assuming $k = 2$ and using $N = 18$, $\omega_A = \Omega_1 = \Omega_2 = 2u_e$, $\gamma_1 = \frac{1}{2}u_e$, where u_e stands for any energy unit ($\hbar = 1$).

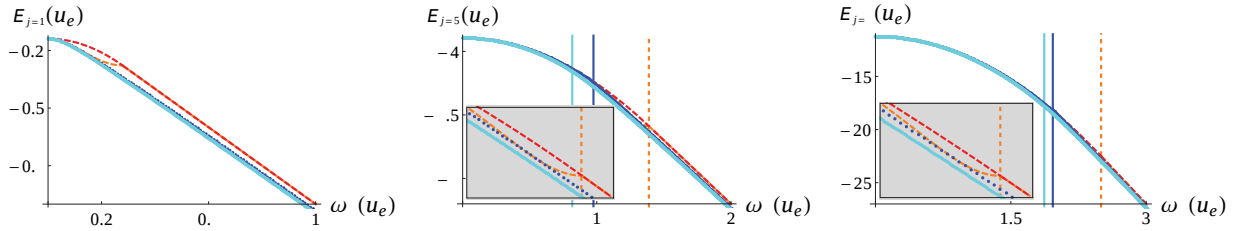

Figure 3.2: Energy of the ground state as a function of ω_A obtained using CS (red), SAS with CS's minima (orange), SAS minimized numerically (blue) and quantum solution (cyan). Vertical lines show the transition according to the quantum solution via fidelity's minimum (cyan), SAS minimized numerically (blue) and SAS with CS's minima (orange). Left: j=1, center: j=5, right: j=9. Assuming $k = 2$ and using $N = 18$, $\Omega_1 = \Omega_2 = 2u_e$, $\gamma_1 = \frac{1}{2}u_e$, $\gamma_2 = 1u_e$, where u_e stands for any energy unit ($\hbar = 1$).

where we have defined $\delta = \dfrac{N\omega_A}{8j\varsigma}$ with $\varsigma = \displaystyle\sum_{\imath=1}^{k} \frac{\gamma_\imath^2}{\Omega_\imath}$. Using the information of this coherent ground state we also obtain the expectation values of the atomic relative population operator J_z and of the number of photons of mode $\imath$ operator $\nu_\imath := a_\imath^\dagger a_\imath$:

$$\langle J_z \rangle_{CS} (\omega_A, \gamma_\imath) = \begin{cases} -j & , \quad \text{for } \delta \geq 1 \\ -j\delta & , \quad \text{for } \delta < 1, \end{cases} \tag{3.3}$$

$$\langle \nu_\imath \rangle_{CS} (\omega_A, \gamma_\imath, \gamma_\jmath) = \begin{cases} 0 & , \quad \text{for } \delta \geq 1 \\ \dfrac{\gamma_\imath^2}{\Omega_\imath^2} \dfrac{j\omega_A}{2\varsigma} \left(\dfrac{1}{\delta} - \delta \right) & , \quad \text{for } \delta < 1. \end{cases} \tag{3.4}$$

Analogously as for the CS's energy surface, the SAS's energy surface is obtained by taking the expectation value of Hamiltonian 2.5 with respect to the state $|\bar{\alpha}, \xi_j\rangle_+$, and has the more complicated form

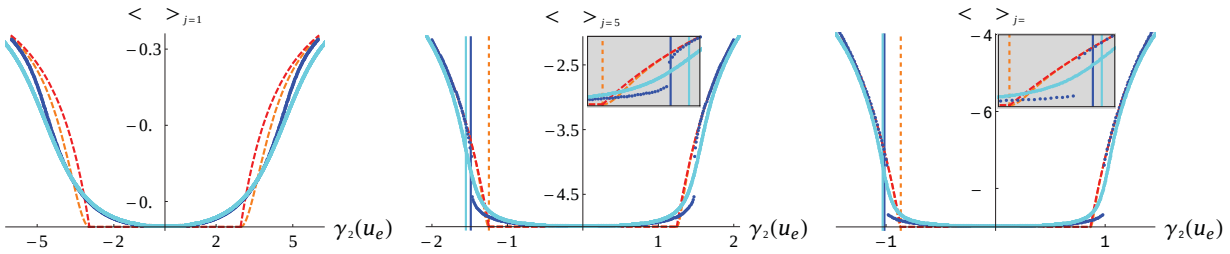

Figure 3.3: Expectation value of J_z as a function of γ_2 obtained using CS (red), SAS with CS's minima (orange), SAS minimized numerically (blue) and quantum solution (cyan). Vertical lines show the transition according to the quantum solution via fidelity's minimum (cyan), SAS minimized numerically (blue) and SAS with CS's minima (orange). Left: j=1, center: j=5, right: j=9. Assuming $k = 2$ and using $N = 18$, $\omega_A = \Omega_1 = \Omega_2 = 2u_e$, $\gamma_1 = \frac{1}{2}u_e$, where u_e stands for any energy unit ($\hbar = 1$).

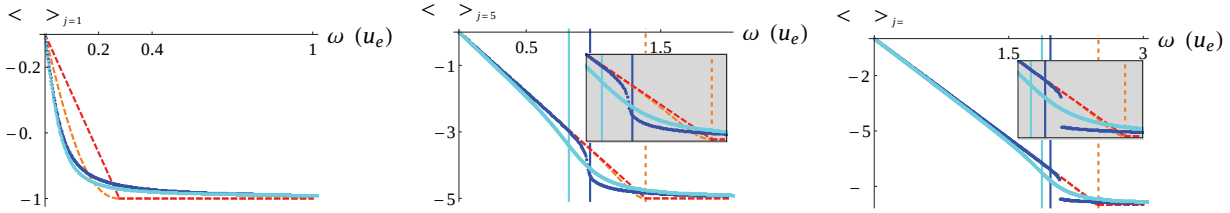

Figure 3.4: Expectation value of J_z as a function of ω_A obtained using CS (red), SAS with CS's minima (orange), SAS minimized numerically (blue) and quantum solution (cyan). Vertical lines show the transition according to the quantum solution via fidelity's minimum (cyan), SAS minimized numerically (blue) and SAS with CS's minima (orange). Left: j=1, center: j=5, right: j=9. Assuming $k = 2$ and using $N = 18$, $\Omega_1 = \Omega_2 = 2u_e$, $\gamma_1 = \frac{1}{2}u_e$, $\gamma_2 = 1u_e$, where u_e stands for any energy unit ($\hbar = 1$).

$$\begin{aligned}\mathcal{H}_{j,SAS}\left(q_\imath, p_\imath, \theta, \phi\right) &:= \left\langle \bar{\alpha}, \xi_j \right|_+ H \left| \bar{\alpha}, \xi_j \right\rangle_+ \\ &= \left(\frac{1 + E\left(-\cos\theta\right)^{2j-2}}{1 + E\left(-\cos\theta\right)^{2j}}\right)\left(-j\omega_A \cos\theta\right) \\ &+ \left(\frac{1 - E\left(-\cos\theta\right)^{2j}}{1 + E\left(-\cos\theta\right)^{2j}}\right)\sum_{\ell=1}^{k}\Omega_\ell\left(q_\ell^2 + p_\ell^2\right) \\ &- \frac{4j}{\sqrt{N}}\sin\theta\sum_{\ell=1}^{k}\left\{\frac{\cos\phi\gamma_\ell q_\ell + E\left(-\cos\theta\right)^{2j-1}\sin\phi\gamma_\ell p_\ell}{1 + E\left(-\cos\theta\right)^{2j}}\right\}. \end{aligned} \tag{3.5}$$

As a first approximation, we may substitute the critical values obtained for the CS's energy surface into (3.5), we obtain the trial state which approximates the lowest symmetry-adapted energy state, and with respect to which we evaluate the expectation values of the observables H, J_z and $\nu_\imath$:

$$\mathcal{E}_{SAS}\left(\omega_A, \gamma_\imath\right) = \begin{cases} -j\omega_A & , \text{for } \delta \geq 1 \\ -j\omega_A\left[\delta\left(\dfrac{1 + \varepsilon\left(-\delta\right)^{2j-2}}{1 + \varepsilon\left(-\delta\right)^{2j}}\right) + \dfrac{1}{2}\left(\dfrac{1}{\delta} - \delta\right)\right] & , \text{for } \delta < 1, \end{cases} \tag{3.6}$$

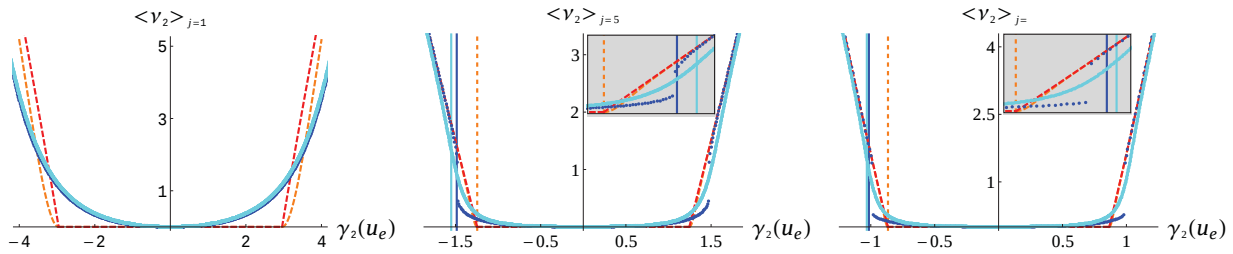

Figure 3.5: Expectation value of $\nu_2 = a_2^\dagger a_2$ as a function of γ_2 obtained using CS (red), SAS with CS's minima (orange), SAS minimized numerically (blue) and quantum solution (cyan). Vertical lines show the transition according to the quantum solution via fidelity's minimum (cyan), SAS minimized numerically (blue) and SAS with CS's minima (orange). Left: j=1, center: j=5, right: j=9. Assuming $k = 2$ and using $N = 18$, $\omega_A = \Omega_1 = \Omega_2 = 2u_e$, $\gamma_1 = \frac{1}{2}u_e$, where u_e stands for any energy unit ($\hbar = 1$).

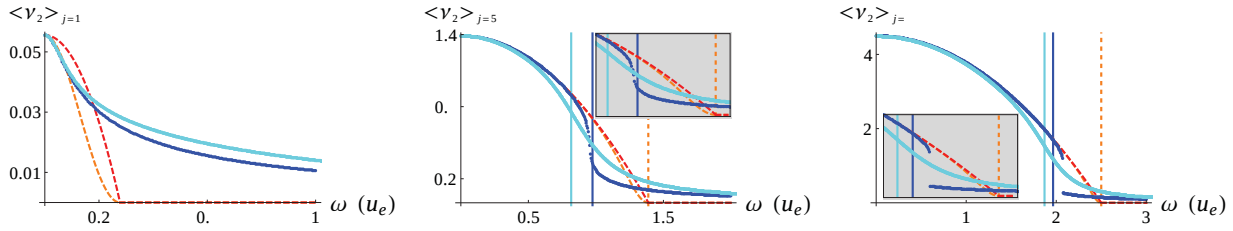

Figure 3.6: Expectation value of $\nu_2 = a_2^\dagger a_2$ as a function of ω_A obtained using CS (red), SAS with CS's minima (orange), SAS minimized numerically (blue) and quantum solution (cyan). Vertical lines show the transition according to the quantum solution via fidelity's minimum (cyan), SAS minimized numerically (blue) and SAS with CS's minima (orange). Left: j=1, center: j=5, right: j=9. Assuming $k = 2$ and using $N = 18$, $\Omega_1 = \Omega_2 = 2u_e$, $\gamma_1 = \frac{1}{2}u_e$, $\gamma_2 = 1u_e$, where u_e stands for any energy unit ($\hbar = 1$).

$$\langle J_z \rangle_{SAS}(\omega_A, \gamma_i) = \begin{cases} -j & , \quad \text{for } \delta \geq 1 \\ -j\delta \left(\dfrac{1 + \varepsilon (-\delta)^{2j-2}}{1 + \varepsilon (-\delta)^{2j}} \right) & , \quad \text{for } \delta < 1, \end{cases} \tag{3.7}$$

$$\langle \nu_i \rangle_{SAS}(\omega_A, \gamma_i, \gamma_j) = \begin{cases} 0 & , \quad \text{for } \delta \geq 1 \\ \dfrac{\gamma_i^2}{\Omega_i^2} \dfrac{j\omega_A}{2\varsigma} \left(\dfrac{1}{\delta} - \delta \right) \left(\dfrac{1 - \varepsilon (-\delta)^{2j}}{1 + \varepsilon (-\delta)^{2j}} \right) & , \quad \text{for } \delta < 1, \end{cases} \tag{3.8}$$

where $\varepsilon = \exp\left\{ \dfrac{-j\omega_A \sigma}{\varsigma} \right\}$ with $\sigma = \sum_{i=1}^{k} \dfrac{\gamma_i^2}{\Omega_i^2}$.

Of course, we can minimize eq. (3.5) numerically for the SAS and obtain the expectation value of the relevant matter and field observables. In our numerical analysis we study the case with two modes of the radiation field, as it is the maximum number of orthogonal modes that can be present in a 3D cavity with the restrictions that the modes interact with the electric dipole moment of the atoms and to be in resonance with the frequency associated with the energy difference between the two levels of the atoms. This latter restriction is just considered to have the maximum transition probability between states.

For the exact quantum solution we must resort to numerical diagonalization of the Hamiltonian and use the lowest eigenstate to compute the expectation values of the relevant observables.

The results, properties of the ground state related to the CS, those related to the SAS using the critical points of the CS (which have the advantage of also providing analytical solutions), those of the SAS minimized

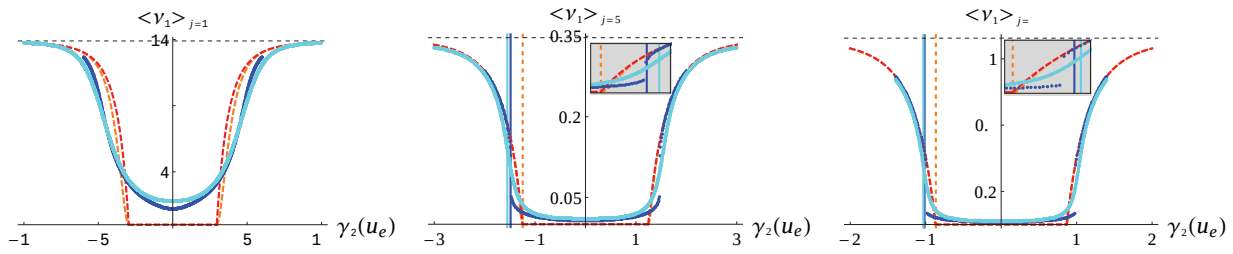

Figure 3.7: Expectation value of $\nu_1 = a_1^\dagger a_1$ as a function of γ_2 obtained using CS (red), SAS with CS's minima (orange), SAS minimized numerically (blue) and quantum solution (cyan). Horizontal dashed line shows the asymptote of $\langle \nu_1 \rangle$ at $\frac{4j^2\gamma_1^2}{N\Omega_1^2}$. Vertical lines show the transition according to the quantum solution via fidelity's minimum (cyan), SAS minimized numerically (blue) and SAS with CS's minima (orange). Left: j=1, center: j=5, right: j=9. Assuming $k = 2$ and using $N = 18$, $\omega_A = \Omega_1 = \Omega_2 = 2u_e$, $\gamma_1 = \frac{1}{2}u_e$, where u_e stands for any energy unit ($\hbar = 1$).

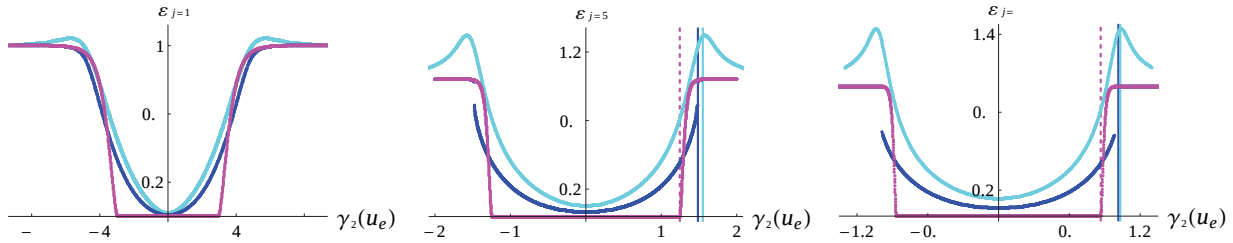

Figure 3.8: Entropy of entanglement as a function of γ_2 obtained SAS with CS's minima (magenta), SAS minimized numerically (blue) and quantum solution (cyan). Vertical lines show the transition according to the quantum solution via fidelity's minimum (cyan), SAS minimized numerically (blue) and SAS with CS's minima (magenta). Left: j=1, center: j=5, right: j=9. Assuming $k = 2$ and using $N = 18$, $\omega_A = \Omega_1 = \Omega_2 = 2u_e$, $\gamma_1 = \frac{1}{2}u_e$, where u_e stands for any energy unit ($\hbar = 1$).

numerically and those of the quantum solution through numerical diagonalization, are shown in figures 3.1 - 3.15 and are discussed below.

One advantage of having analytical solutions is, of course, that the order of the transition may be easily found. Equations (3.2) and (3.6) show a second-order QPT at $\delta = \frac{N\omega_A}{8j\varsigma} = 1$ with the CS and SAS using CS's minima (SAScs) approximations. In figure 3.1 it can be seen that the data of the SAS using numerical minimization (SASn) has a small discontinuity (the QPT) at $\gamma_2 \approx 1.485$ for $j = 5$ and $\gamma_2 \approx 1.015$ for $j = 9$, while in figure 3.2 this discontinuity is at $\omega_A \approx 0.975$ for $j = 5$ and $\omega_A \approx 1.965$ for $j = 9$. Note that the SASn solution always approximate better the exact quantum result, as the cooperation number increases this approximation gets better, in fact, for $2j = 18 = N$ the loci of the separatrix between the normal and collective regions for the quantum and SASn solutions are indistinguishable (except in the zoomed inset). The true loci of the QPT may be found through the fidelity: figures 3.10 and 3.11 show the fidelity between neighboring states of the quantum solution, where the exact QPT is characterized by the minimum, which is localized at $\gamma_2 \approx 1.550$ for $j = 5$, $\gamma_2 \approx 1.031$ for $j = 9$ in figure 3.10; and $\omega_A \approx 0.817$ for $j = 5$, $\omega_A \approx 1.870$ for $j = 9$ in figure 3.11.

The discrepancies between the transition values of the SAScs approximation and the exact quantum solution become obvious when looking at figures 3.12 and 3.13, where the fidelity between SAScs and the quantum solution drops (and oscillates) in a vicinity of the separatrix. Therefore, we conclude that SAScs

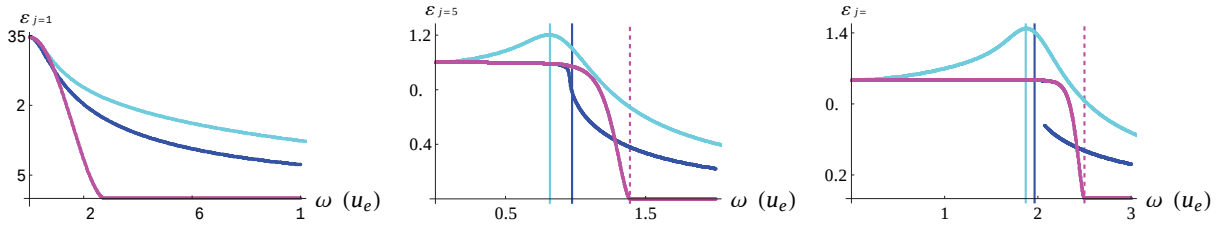

Figure 3.9: Entropy of entanglement as a function of ω_A obtained SAS with CS's minima (magenta), SAS minimized numerically (blue) and quantum solution (cyan). Vertical lines show the transition according to the quantum solution via fidelity's minimum (cyan), SAS minimized numerically (blue) and SAS with CS's minima (magenta). Left: j=1, center: j=5, right: j=9. Assuming $k = 2$ and using $N = 18$, $\Omega_1 = \Omega_2 = 2u_e$, $\gamma_1 = \frac{1}{2}u_e$, $\gamma_2 = 1u_e$, where u_e stands for any energy unit ($\hbar = 1$).

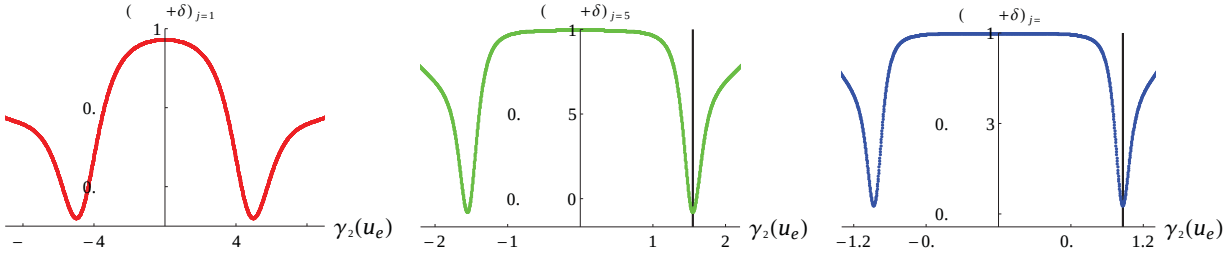

Figure 3.10: Fidelity between neighboring quantum states as a function of γ_2. Left: j=1, center: j=5, right: j=9. Assuming $k = 2$ and using $N = 18$, $\omega_A = \Omega_1 = \Omega_2 = 2u_e$, $\gamma_1 = \frac{1}{2}u_e$, where u_e stands for any energy unit ($\hbar = 1$). Vertical black line shows the fidelity's minimum (i.e. the quantum phase transition) for $j = 5$ and $j = 9$.

offer a good approximation (with an analytic expression) to the exact quantum solution far from the QPT for low cooperation numbers, but as $j \to \infty$, the interval where the SASc fail to reproduce the correct behavior, becomes smaller.

Figures 3.14 and 3.15 show the fidelity drop at the separatrix for the SASn. The resemblance to figures 3.10 and 3.11 is uncanny, showing the benefits of restoring the Hamiltonian symmetry into the trial variational states. This improvement comes with the disadvantage of losing the analytic expression, but still has an advantage over the quantum solution: the computational time. SASn are obtained by numerically minimizing a real function, which is far easier to do (computationally speaking) than numerically diagonalizing the Hamiltonian matrix.

Figures 3.1 - 3.7 show the comparison between the different approximations to the ground state: CS, SASc, SASn and quantum solution. We show the behavior of $\mathcal{E} := \langle H \rangle$, $\langle J_z \rangle$ and $\langle \nu_\iota \rangle$ as functions of the atomic frequency ω_A and one of the coupling constants γ_2, for different cooperation numbers. It can be noticed that the discontinuity in the second derivative of the energy (as modeled with CS and SASc) translates into a discontinuity in the first derivative of $\langle J_z \rangle$ and $\langle \nu_\iota \rangle$, thus characterizing the QPT by means of an abrupt change in the expectation values of the observables. In general, it can be observed that the four methods (CS, SASc, SASn and quantum solution) converge in the limit $\delta \to 0$, where the case $j \to \infty$ is particularly interesting as the interval around the QPT, where all the approximations fail to reproduce the correct behavior, becomes smaller.

It is worth mentioning the significance and importance of figures 3.7 and 3.16 as they show aspects of

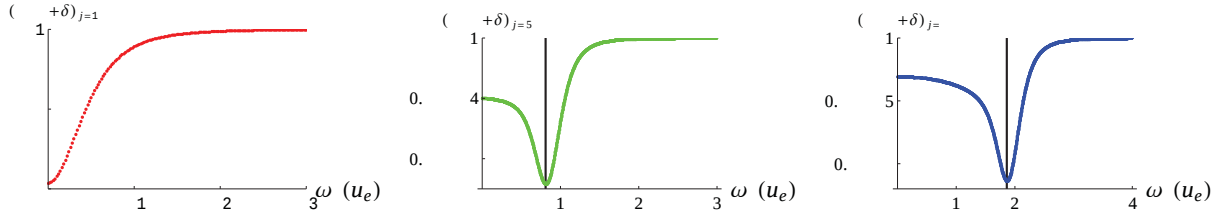

Figure 3.11: Fidelity between neighboring quantum states as a function of ω_A. Left: j=1, center: j=5, right: j=9. Assuming $k = 2$ and using $N = 18$, $\Omega_1 = \Omega_2 = 2u_e$, $\gamma_1 = \frac{1}{2}u_e$, $\gamma_2 = 1u_e$, where u_e stands for any energy unit ($\hbar = 1$). Vertical black line shows the fidelity's minimum (i.e. the quantum phase transition) for $j = 5$ and $j = 9$.

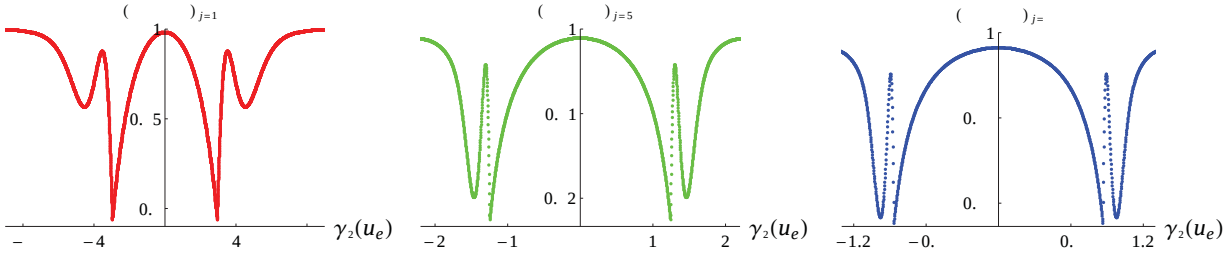

Figure 3.12: Fidelity between SAS with CS's minima and quantum solution as a function of γ_2. Up (left): j=1, up (right): j=5, down: j=9. Assuming $k = 2$ and using $N = 18$, $\omega_A = \Omega_1 = \Omega_2 = 2u_e$, $\gamma_1 = \frac{1}{2}u_e$, where u_e stands for any energy unit ($\hbar = 1$).

the multi-mode Dicke model which are not present in the single-mode case. In figure 3.7 it is shown how the different modes of radiation (orthogonal in principle) interact through the matter field, analogously as it occurs with different atoms interacting through the radiation field. On the other hand, figure 3.16 shows (pictorically) the phase diagrams of the two-mode system, in which it can be observed that any two points in the super-radiant region can be joined by a trajectory that does not cross the normal region, a characteristic that the single-mode system does not have.

Figures 3.8 and 3.9 show the comparison between SASc, SASn and the quantum solution for the entropy of entanglement S_ε as a function of the atomic frequency ω_A and one of the coupling constants γ_2, using different cooperation numbers. A characterization of the QPT can be made by observing that the entropy of entanglement obtained using the quantum solution shows a maximum at the transition, an attribute that SASc and SASn approximations fail to reproduce.

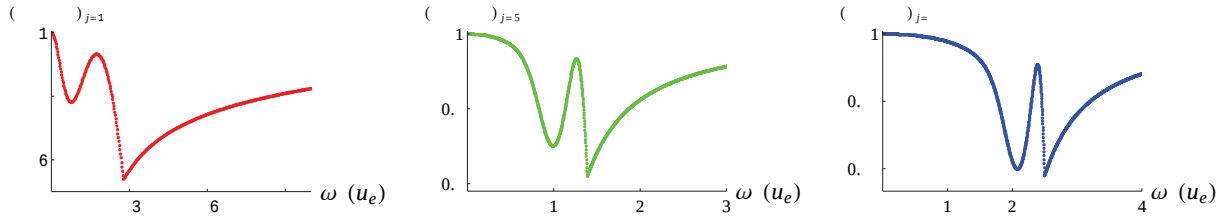

Figure 3.13: Fidelity between SAS with CS's minima and quantum solution as a function of ω_A. Up (left): j=1, up (right): j=5, down: j=9. Assuming $k = 2$ and using $N = 18$, $\Omega_1 = \Omega_2 = 2u_e$, $\gamma_1 = \frac{1}{2}u_e$, $\gamma_2 = 1u_e$, where u_e stands for any energy unit ($\hbar = 1$).

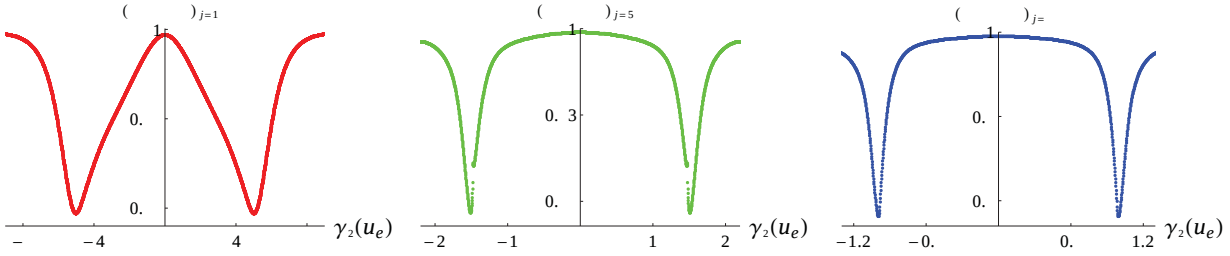

Figure 3.14: Fidelity between SAS minimized numerically and quantum solution as a function of γ_2. Up: j=1, center: j=5, down: j=9. Assuming $k = 2$ and using $N = 18$, $\omega_A = \Omega_1 = \Omega_2 = 2u_e$, $\gamma_1 = \frac{1}{2}u_e$, where u_e stands for any energy unit ($\hbar = 1$).

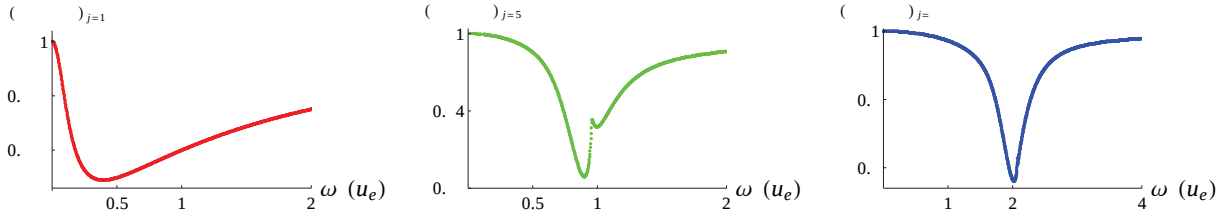

Figure 3.15: Fidelity between SAS minimized numerically and quantum solution as a function of ω_A. Up: j=1, center: j=5, down: j=9. Assuming $k = 2$ and using $N = 18$, $\Omega_1 = \Omega_2 = 2u_e$, $\gamma_1 = \frac{1}{2}u_e$, $\gamma_2 = 1u_e$, where u_e stands for any energy unit ($\hbar = 1$).

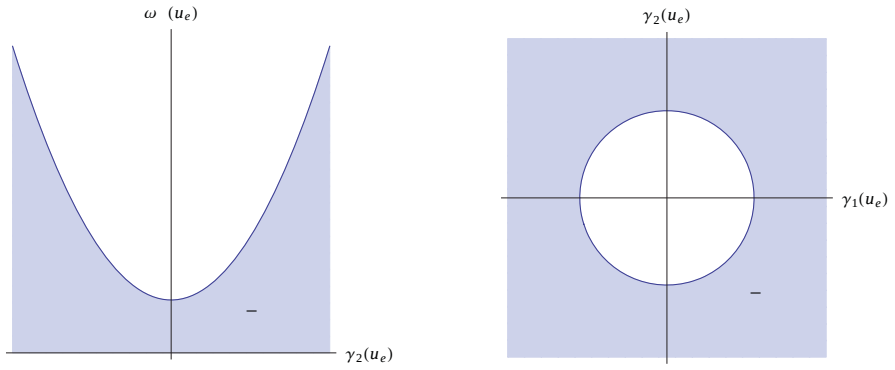

Figure 3.16: Pictographic representation of the phase diagrams in the plane (γ_2, ω_A) (up) and (γ_1, γ_2) (down) obtained using CS. Normal region (white) is defined as the region where $\delta \geq 1$ and super-radiant region (light blue) is defined as the region where $\delta < 1$. u_e stands for any energy unit ($\hbar = 1$).

3.2 Three-level Atoms

3.2.1 Observables and Fidelities: Ξ Configuration

The results presented in this section correspond to the analysis made with the atoms of the system being in the Ξ configuration. Results for the Λ and V configurations are shown in the appendix.

As it has already been stated, the energy surface minimization was carried out numerically; figures 3.17 and 3.18 show the results of this procedure. In them, the average ground-state's energy of the system is plotted as a function of the dipolar coupling parameters μ_{12} and μ_{23} for all the four possible representations and cooperation numbers available for $N = 4$. It can be seen from these figures that the area of the normal region (shown in dark gray) in the μ_{ij} plane gets larger as n_c gets smaller; this is consistent with the intuition behind the cooperation number as the fewer the effective number of atoms is, the stronger the required coupling needs to be for the system to reach the super-radiant phase (please note the different scale of each figure).

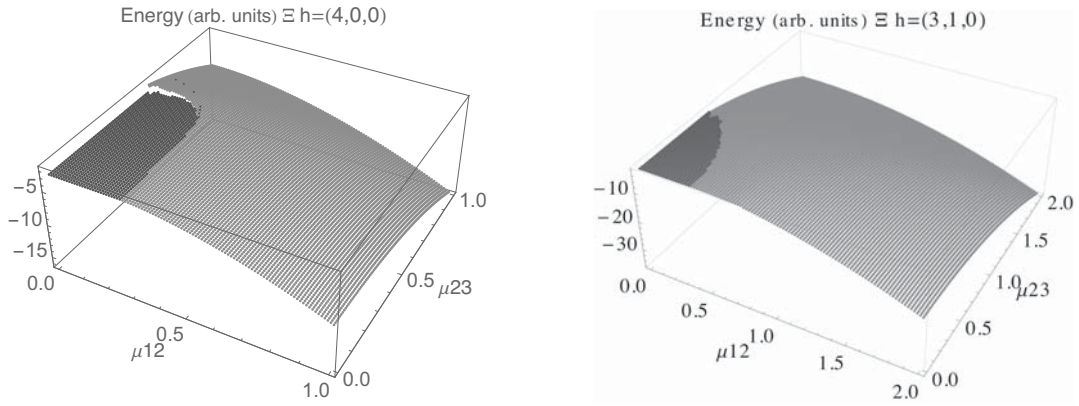

Figure 3.17: 3D plot of the energy of the coherent ground state as a function of the coupling parameters μ_{12} and μ_{23}. The dark-gray region represents the normal (sub-radiant) phase of the system. Both figures were obtained using $\omega_1 = 1.\bar{3}$, $\omega_2 = 1.\bar{6}$, $\Omega = 0.5$ and correspond to the Ξ configuration. Left: $h = (4, 0, 0)$, Right: $h = (3, 1, 0)$. Units are arbitrary but the same for all non-dimensionless quantities ($\hbar = 1$).

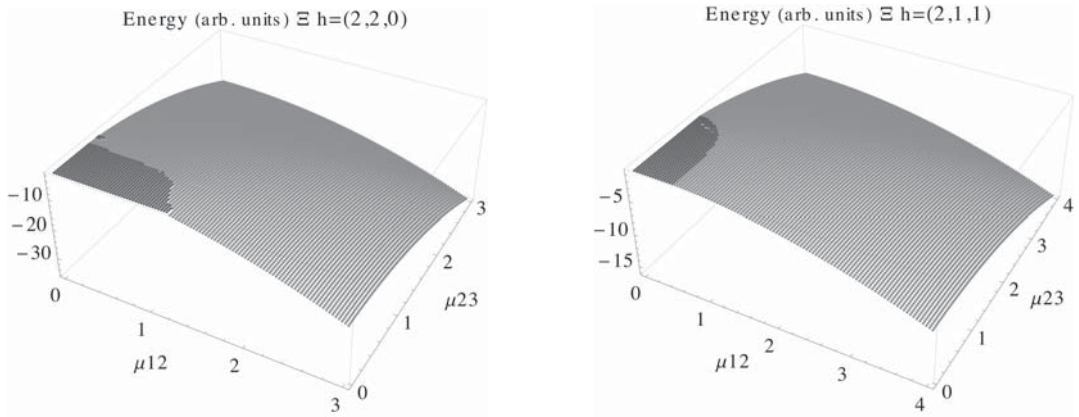

Figure 3.18: 3D plot of the energy of the coherent ground state as a function of the coupling parameters μ_{12} and μ_{23}. The dark-gray region represents the normal (sub-radiant) phase of the system. Both figures were obtained using $\omega_1 = 1.\bar{3}$, $\omega_2 = 1.\bar{6}$, $\Omega = 0.5$ and correspond to the Ξ configuration. Left: $h = (2, 2, 0)$, Right: $h = (2, 1, 1)$. Units are arbitrary but the same for all non-dimensionless quantities ($\hbar = 1$).

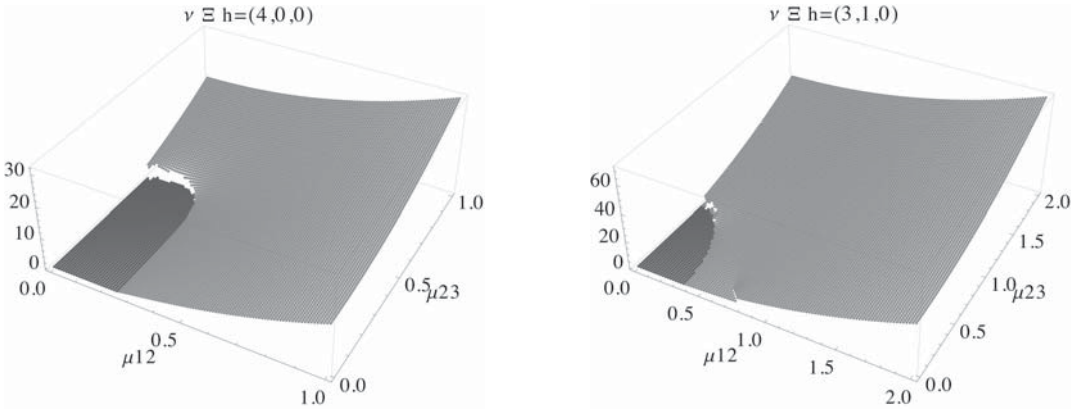

Figure 3.19: 3D plot of the average number of photons in the coherent ground state as a function of the coupling parameters μ_{12} and μ_{23}. The dark-gray region represents the normal (sub-radiant) phase of the system. Both figures were obtained using $\omega_1 = 1.\bar{3}$, $\omega_2 = 1.\bar{6}$, $\Omega = 0.5$ and correspond to the Ξ configuration. Left: $h = (4, 0, 0)$, Right: $h = (3, 1, 0)$. Units are arbitrary but the same for all non-dimensionless quantities ($\hbar = 1$).

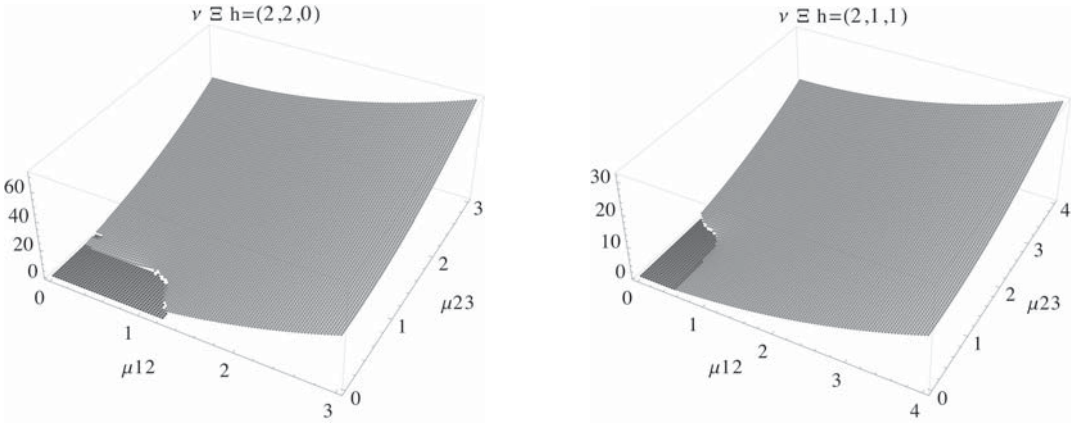

Figure 3.20: 3D plot of the average number of photons in the coherent ground state as a function of the coupling parameters μ_{12} and μ_{23}. The dark-gray region represents the normal (sub-radiant) phase of the system. Both figures were obtained using $\omega_1 = 1.\bar{3}$, $\omega_2 = 1.\bar{6}$, $\Omega = 0.5$ and correspond to the Ξ configuration. Left: $h = (2, 2, 0)$, Right: $h = (2, 1, 1)$. Units are arbitrary but the same for all non-dimensionless quantities ($\hbar = 1$).

Figures 3.19 and 3.20 display the average number of photons in the ground state of the system, which in the normal region is zero but grows rapidly as we go deeper into the super-radiant phase. This growth has been shown to be of fourth order with respect to the dipolar coupling parameters for two-level systems in section 3.1.

The atomic observables are studied in figures 3.21 to 3.24, they show both the average of half the population difference between the second and first levels, and the average of half the population difference between the third and second levels, which correspond respectively to the expectation value, in the ground state, of the Jz_1 and Jz_2 operators. These figures reflect one of the features that make representation theory and the Gelfand-Tsetlin labeling scheme useful tools to describe this kind of systems: notice that the parameters h_1, h_2 and h_3 represent, respectively, the atomic population of the first, second and third level, in the normal region of the system.

As the methodology used in this work provides an approximation to the ground state, a comparison

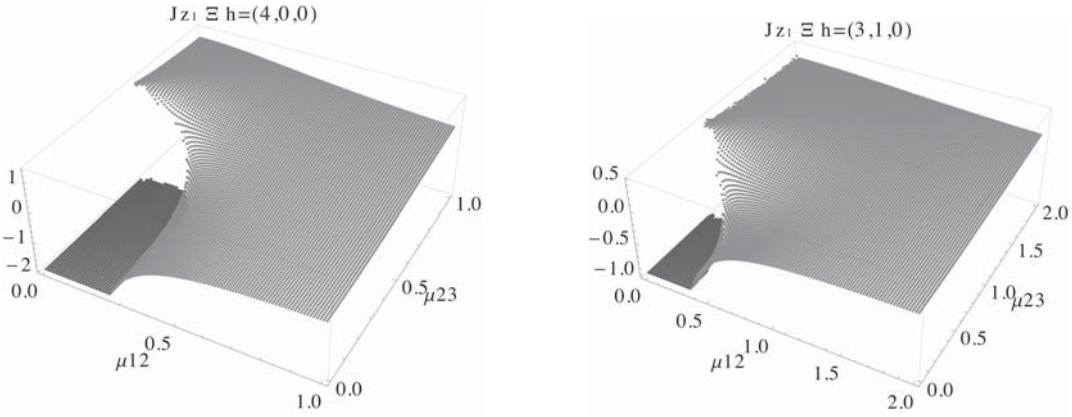

Figure 3.21: 3D plot of the expectation value of the Jz_1 operator (half the population difference between the second and first levels) in the coherent ground state as a function of the coupling parameters μ_{12} and μ_{23}. The dark-gray region represents the normal (sub-radiant) phase of the system. Both figures were obtained using $\omega_1 = 1.\bar{3}$, $\omega_2 = 1.\bar{6}$, $\Omega = 0.5$ and correspond to the Ξ configuration. Left: $h = (4, 0, 0)$, Right: $h = (3, 1, 0)$. Units are arbitrary but the same for all non-dimensionless quantities ($\hbar = 1$).

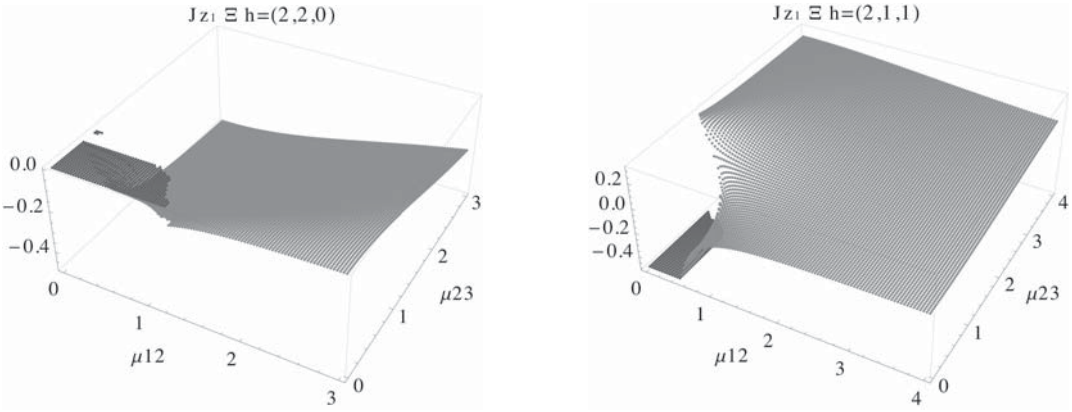

Figure 3.22: 3D plot of the expectation value of the Jz_1 operator (half the population difference between the second and first levels) in the coherent ground state as a function of the coupling parameters μ_{12} and μ_{23}. The dark-gray region represents the normal (sub-radiant) phase of the system. Both figures were obtained using $\omega_1 = 1.\bar{3}$, $\omega_2 = 1.\bar{6}$, $\Omega = 0.5$ and correspond to the Ξ configuration. Left: $h = (2, 2, 0)$, Right: $h = (2, 1, 1)$. Units are arbitrary but the same for all non-dimensionless quantities ($\hbar = 1$).

between this and the real quantum solution, calculated by explicitly diagonalizing the Hamiltonian matrix, is presented in figures 3.25 to 3.28 by means of the fidelity between them $F(Coh, Q)$, along with the real QPTs obtained using the fidelity between neighboring quantum states $F(Q, Q)$, which we are using to characterize the real QPT.

It is worth mentioning that, in this case, there are mainly two ways in which we can calculate $F(Q, Q)$, one is to compare states along a horizontal line in the (μ_{12}, μ_{23}) plane and the other is to do it along a vertical line, the first method being particularly sensible to vertical QPTs and the second method to horizontal ones. In this work, as both approaches looked almost identical, we decided to only show the resulting plots of one of them. It is important to point out, however, that this decision made continuous lines to look somehow dashed in some parts of our Fidelity (Q,Q) plots.

Some interesting characteristics of the system arise from the results displayed on these figures, the most notorious one being the fact that in the normal region $F(Coh, Q) \approx 1$, meaning both solutions are nearly

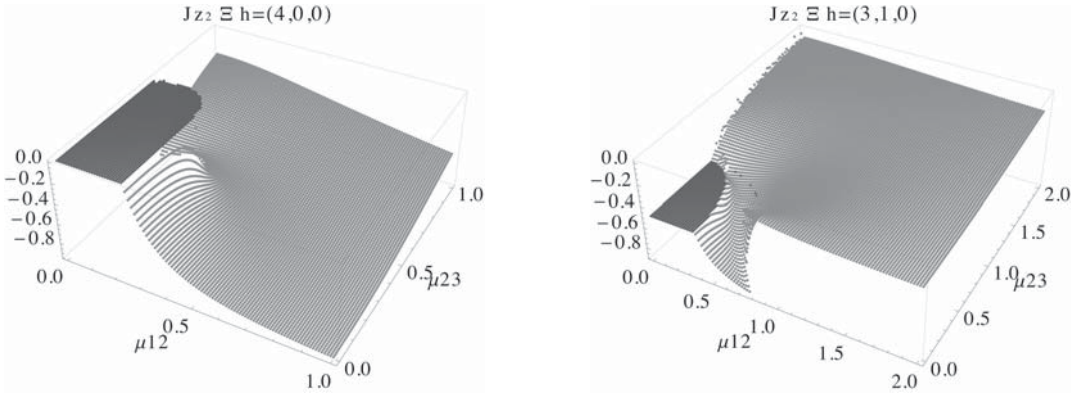

Figure 3.23: 3D plot of the expectation value of the Jz_2 operator (half the population difference between the third and second levels) in the coherent ground state as a function of the coupling parameters μ_{12} and μ_{23}. The dark-gray region represents the normal (sub-radiant) phase of the system. Both figures were obtained using $\omega_1 = 1.\bar{3}$, $\omega_2 = 1.\bar{6}$, $\Omega = 0.5$ and correspond to the Ξ configuration. Left: $h = (4, 0, 0)$, Right: $h = (3, 1, 0)$. Units are arbitrary but the same for all non-dimensionless quantities ($\hbar = 1$).

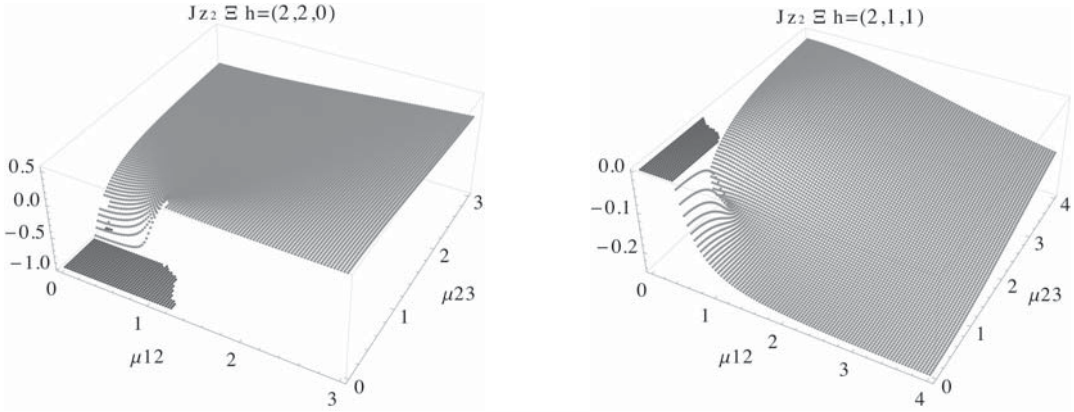

Figure 3.24: 3D plot of the expectation value of the Jz_2 operator (half the population difference between the third and second levels) in the coherent ground state as a function of the coupling parameters μ_{12} and μ_{23}. The dark-gray region represents the normal (sub-radiant) phase of the system. Both figures were obtained using $\omega_1 = 1.\bar{3}$, $\omega_2 = 1.\bar{6}$, $\Omega = 0.5$ and correspond to the Ξ configuration. Left: $h = (2, 2, 0)$, Right: $h = (2, 1, 1)$. Units are arbitrary but the same for all non-dimensionless quantities ($\hbar = 1$).

identical there. However, near the coherent QPT the fidelity starts falling rapidly until it reaches $F(Coh, Q) \approx \frac{1}{2}$ in the super-radiant region; this specific value is not a coincidence, it emerges from a mix of parities the coherent states carry, derived from a symmetry in the total number of excitations of the system. States that respect this symmetry (symmetry-adapted states, or SAS) can be constructed, and have actually already been used to study two- and three-level systems [43] (only for the symmetric representation), as well as other kind of systems [44].

Another interesting aspect of the system present in figures 3.25 to 3.28 is the traces of the coherent QPT present in the Fidelity (Q,Q) plots. These are more noticeable as the cooperation number increases. Traces of the real QPT in the Fidelity (Coh,Q) plots are expected, as this fidelity is literally comparing both kinds of states; however, to see a drop in $F(Q, Q)$ where the coherent QPT occurs is quite a remarkable feature, as there is, in principle, no information about the coherent state approximation in the Fidelity (Q,Q) plots. We attribute this phenomenon to the following two facts: it has been already shown in this thesis, for two-

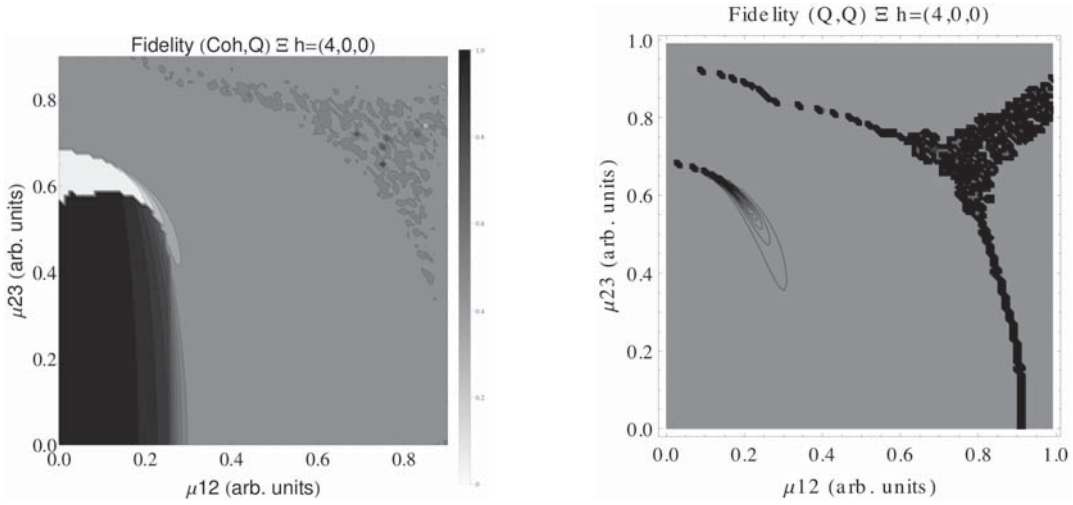

Figure 3.25: Left: Contour plot of the fidelity between coherent states and quantum solution as a function of the coupling parameters μ_{12} and μ_{23}, values range between 0 (white) and 1 (black). Right: Contour plot of the fidelity between neighboring quantum states as a function of the coupling parameters μ_{12} and μ_{23}, black dots represent a drop in the fidelity below 1. Both figures were obtained using $\omega_1 = 1.\bar{3}$, $\omega_2 = 1.\bar{6}$, $\Omega = 0.5$ and correspond to the Ξ configuration in the $h = (4, 0, 0)$ representation. Units are arbitrary but the same for all non-dimensionless quantities ($\hbar = 1$). (Noise in the plots is due to numerical minimization; see text.)

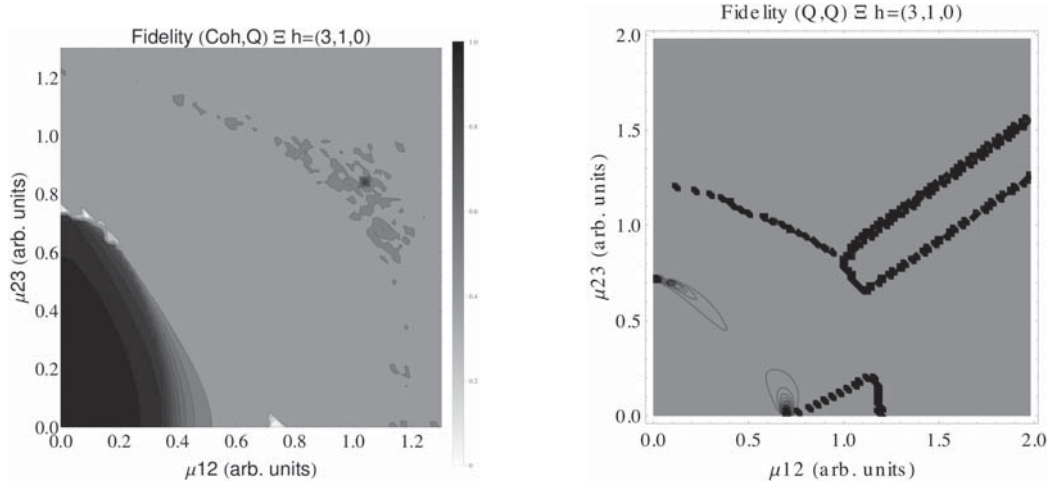

Figure 3.26: Left: Contour plot of the fidelity between coherent states and quantum solution as a function of the coupling parameters μ_{12} and μ_{23}, values range between 0 (white) and 1 (black). Right: Contour plot of the fidelity between neighboring quantum states as a function of the coupling parameters μ_{12} and μ_{23}, black dots represent a drop in the fidelity below 1. Both figures were obtained using $\omega_1 = 1.\bar{3}$, $\omega_2 = 1.\bar{6}$, $\Omega = 0.5$ and correspond to the Ξ configuration in the $h = (3, 1, 0)$ representation. Units are arbitrary but the same for all non-dimensionless quantities ($\hbar = 1$). (Noise in the plots is due to numerical minimization; see text.)

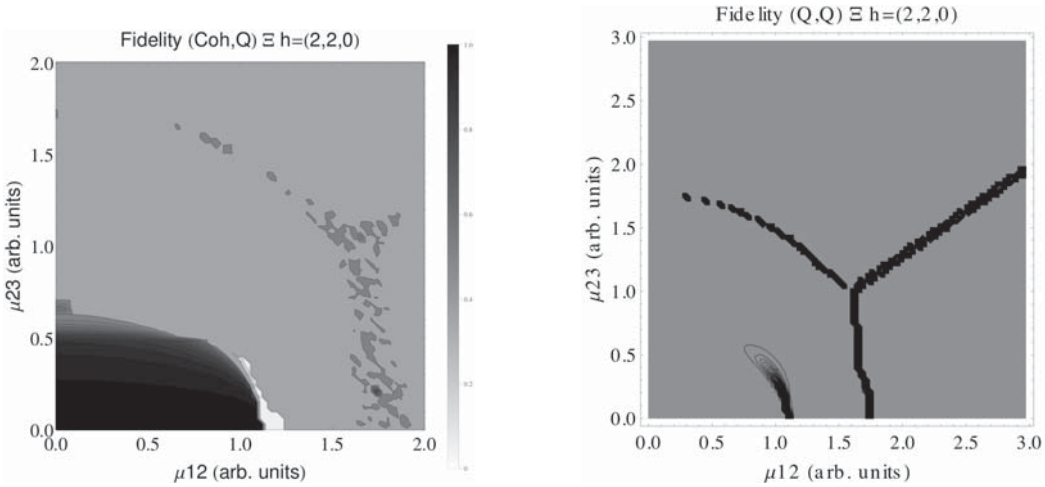

Figure 3.27: Left: Contour plot of the fidelity between coherent states and quantum solution as a function of the coupling parameters μ_{12} and μ_{23}, values range between 0 (white) and 1 (black). Right: Contour plot of the fidelity between neighboring quantum states as a function of the coupling parameters μ_{12} and μ_{23}, black dots represent a drop in the fidelity below 1. Both figures were obtained using $\omega_1 = 1.\bar{3}$, $\omega_2 = 1.\bar{6}$, $\Omega = 0.5$ and correspond to the Ξ configuration in the $h = (2, 2, 0)$ representation. Units are arbitrary but the same for all non-dimensionless quantities ($\hbar = 1$). (Noise in the plots is due to numerical minimization; see text.)

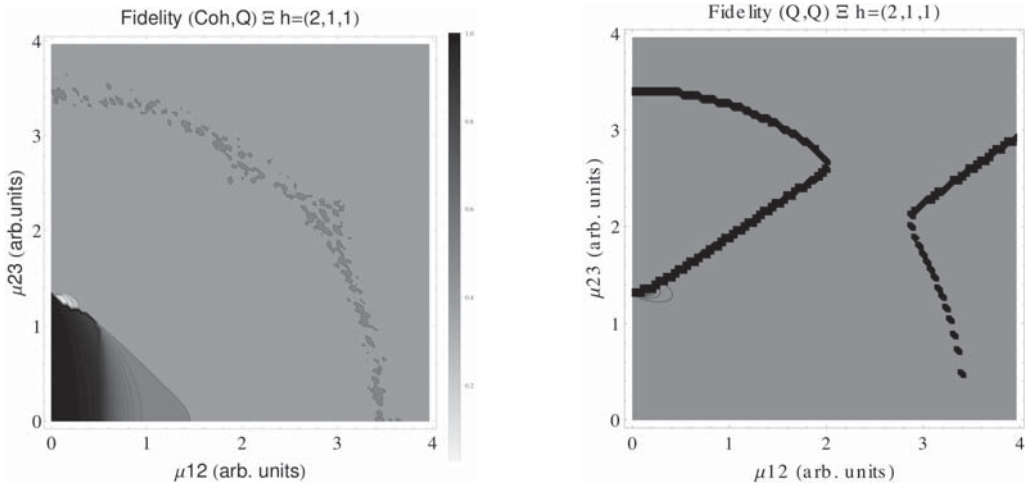

Figure 3.28: Left: Contour plot of the fidelity between coherent states and quantum solution as a function of the coupling parameters μ_{12} and μ_{23}, values range between 0 (white) and 1 (black). Right: Contour plot of the fidelity between neighboring quantum states as a function of the coupling parameters μ_{12} and μ_{23}, black dots represent a drop in the fidelity below 1. Both figures were obtained using $\omega_1 = 1.\bar{3}$, $\omega_2 = 1.\bar{6}$, $\Omega = 0.5$ and correspond to the Ξ configuration in the $h = (2, 1, 1)$ representation. Units are arbitrary but the same for all non-dimensionless quantities ($\hbar = 1$). (Noise in the plots is due to numerical minimization; see text.)

level systems, that the quantum and the SAS solution coincide in the cooperation-number thermodynamic limit (i.e. $n_c \longrightarrow \infty$); and both coherent and SAS solutions can be made to have the same normal region (minimizing both with the same critical values). This leads us to conclude that, as $n_c \longrightarrow \infty$, the traces of the coherent QPT gradually become the real QPT.

In general, these phase diagrams show a richer structure than those obtained from coherent or symmetry-adapted states. Figure 3.25 shows a *transition band* at its upper right corner, compared to a transition line seen in the previously mentioned phase diagrams. This we may attribute to changes in the parity of the total excitation number. Whereas in the rotating wave approximation the total excitation number is a conserved quantity of the system, when taking the full Hamiltonian, as we do here, only its parity is conserved. Thus, we conjecture that the transition to a different parity takes place in the exact quantum solution across a band which contracts down to a point as the number of atoms and the cooperation number increase. When the rotating wave approximation is considered, the system has been shown to have a triple point for the symmetric representation [12], which is fixed in parameter's space (μ_{12}, μ_{23}), is independent on the number of atoms, and prevails in the thermodynamic limit. This triple point also appears in our Fidelity (Q,Q) plots but, from all other figures analyzed, it does not seem to be relevant in the coherent approximation when the full Hamiltonian is considered.

3.2.2 Entropy of Entanglement: Ξ Configuration

The results presented in this section correspond to the analysis made with the atoms of the system being in the Ξ configuration. Results for the Λ and V configurations are shown in the appendix.

In this work we studied a system, described by the Hamiltonian (2.15), of four three-level atoms interacting with a one-mode electromagnetic field, thus we had four possible representations (and cooperation numbers) of SU(3), namely $h = (4,0,0)$ (the symmetric one), $h = (3,1,0)$, $h = (2,2,0)$ and $h = (2,1,1)$ with a cooperation number of 4, 3, 2 and 1 respectively. We compared the entropy of entanglement to the fidelity between neighboring coherent states as functions of the coupling parameters μ_{ij}. Here, based in the results obtained for two-level systems in section 3.1 , we expected to see a correlation between the coherent quantum phase transition (characterized by the drop in the fidelity) and the region where the entropy of entanglement reaches its highest values.

Results for the atoms being in the Ξ configuration are presented in Figures 3.29–3.32 for all four possible cooperation numbers. The first two graphics (from left to right) show the entropy of entanglement. In them, the region where the entropy reaches its highest values ($S_\varepsilon > 1.02$) is shown in dark gray It is worth noticing that this region gets larger as the cooperation number increases.

The third graphic shows a contour plot of the fidelity between neighboring coherent states. In this, the region where the fidelity drops ($F < 0.97$ is emphasized, although fidelity drops to values near zero) is shown in dark gray. Irregularities appear due to numerical errors in the energy surface's minimization process near the transition.

These graphics suggest the existence of at least two quantum phases at zero temperature for all cooperation numbers; these are the so-called normal and collective regions. Although it has been already shown that this

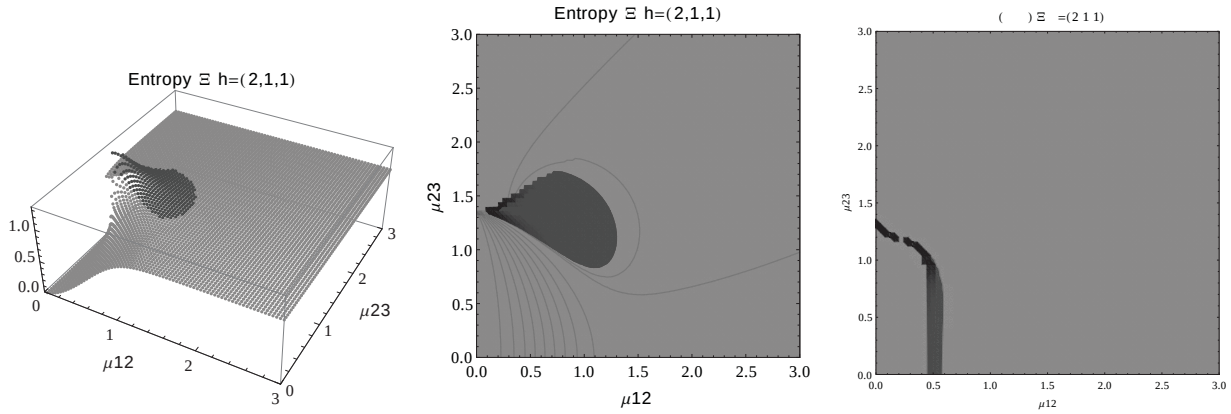

Figure 3.29: (**Left**) 3D plot of the entropy of entanglement as a function of the coupling parameters μ_{12} and μ_{23}, the maximum value of the entropy is $S_\varepsilon = 1.32$ and the region where $S_\varepsilon > 1.02$ is shown in dark gray (**Center**) Contour plot of the entropy of entanglement as a function of the coupling parameters μ_{12} and μ_{23}, the region where $S_\varepsilon > 1.02$ is shown in dark gray (**Right**) Fidelity between neighboring coherent states as a function of the coupling parameters μ_{12} and μ_{23}, dark gray region shows the fidelity's minimum (i.e., the phase transition). All figures use $\omega_1 = 1.\bar{3}$, $\omega_2 = 1.\bar{6}$, $\Omega = 0.5$ and correspond to the Ξ configuration and the $h = (2, 1, 1)$ representation.

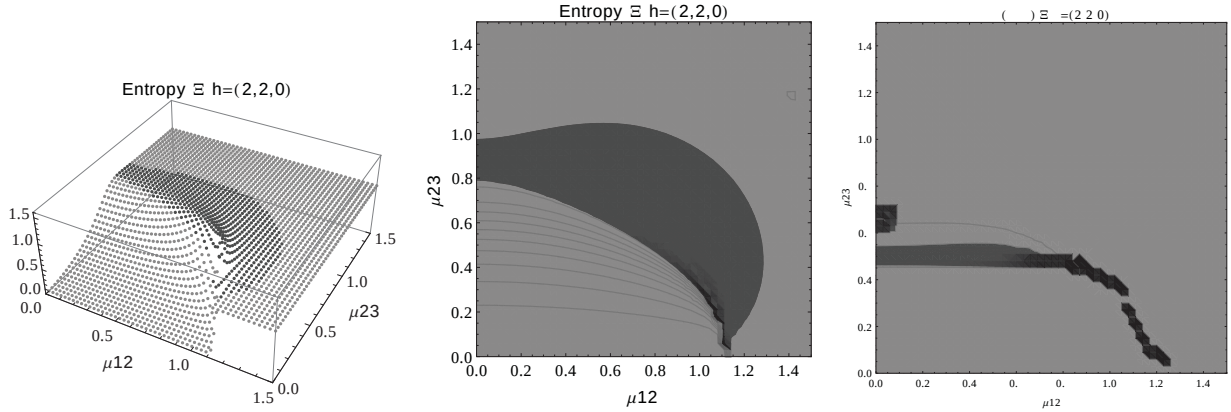

Figure 3.30: (**Left**) 3D plot of the entropy of entanglement as a function of the coupling parameters μ_{12} and μ_{23}, the maximum value of the entropy is $S_\varepsilon = 1.58$ and the region where $S_\varepsilon > 1.02$ is shown in dark gray (**Center**) Contour plot of the entropy of entanglement as a function of the coupling parameters μ_{12} and μ_{23}, the region where $S_\varepsilon > 1.02$ is shown in dark gray (**Right**) Fidelity between neighboring coherent states as a function of the coupling parameters μ_{12} and μ_{23}, dark gray region shows the fidelity's minimum (i.e., the phase transition). All figures use $\omega_1 = 1.\bar{3}$, $\omega_2 = 1.\bar{6}$, $\Omega = 0.5$ and correspond to the Ξ configuration and the $h = (2, 2, 0)$ representation.

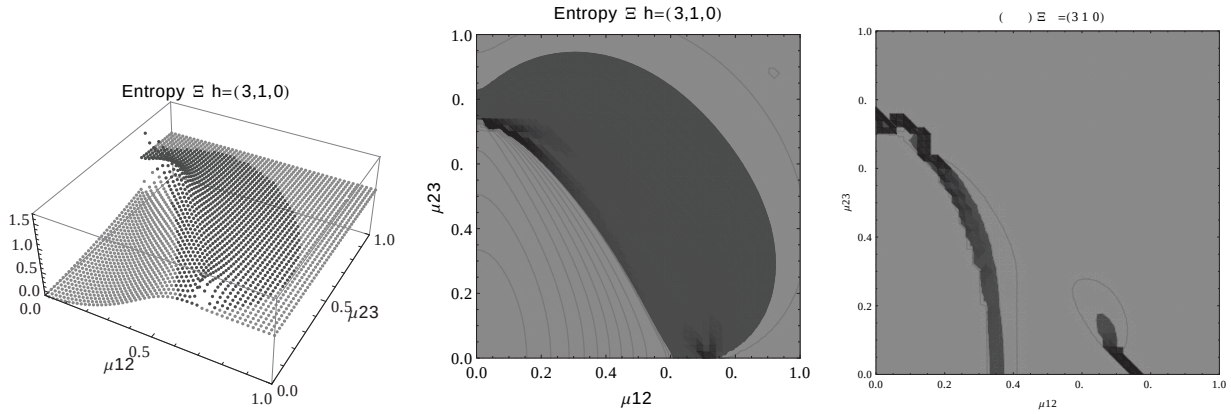

Figure 3.31: (**Left**) 3D plot of the entropy of entanglement as a function of the coupling parameters μ_{12} and μ_{23}, the maximum value of the entropy is $S_\varepsilon = 1.65$ and the region where S_ε >1.02 is shown in dark gray (**Center**) Contour plot of the entropy of entanglement as a function of the coupling parameters μ_{12} and μ_{23}, the region where S_ε >1.02 is shown in dark gray (**Right**) Fidelity between neighboring coherent states as a function of the coupling parameters μ_{12} and μ_{23}, dark gray region shows the fidelity's minimum (i.e., the phase transition). All figures use $\omega_1 = 1.\bar{3}$, $\omega_2 = 1.\bar{6}$, $\Omega = 0.5$ and correspond to the Ξ configuration and the $h = (3, 1, 0)$ representation.

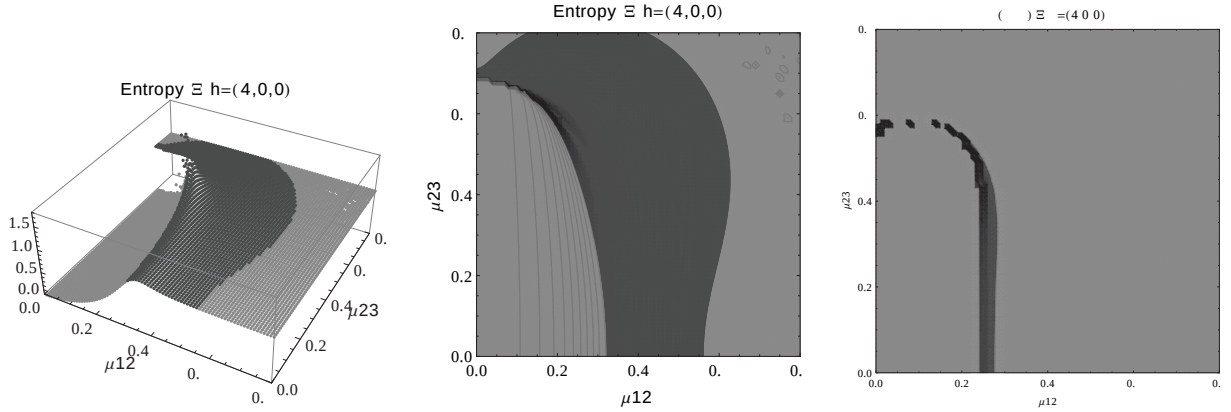

Figure 3.32: (**Left**) 3D plot of the entropy of entanglement as a function of the coupling parameters μ_{12} and μ_{23}, the maximum value of the entropy is $S_\varepsilon = 1.78$ and the region where S_ε >1.02 is shown in dark gray (**Center**) Contour plot of the entropy of entanglement as a function of the coupling parameters μ_{12} and μ_{23}, the region where S_ε >1.02 is shown in dark gray (**Right**) Fidelity between neighboring coherent states as a function of the coupling parameters μ_{12} and μ_{23}, dark gray region shows the fidelity's minimum (i.e., the phase transition). All figures use $\omega_1 = 1.\bar{3}$, $\omega_2 = 1.\bar{6}$, $\Omega = 0.5$ and correspond to the Ξ configuration and the $h = (4, 0, 0)$ representation.

configuration has a triple point (i.e., three phases) in the symmetric representation [12], the discrepancy leads us to conclude that the entropy of entanglement is just sensitive to the transition between normal and super-radiant phases but not between possible transitions within these regions.

An interesting feature we can observe in these graphics, is that of an increase in the sensitivity of the entropy of entanglement as the cooperation number tends to the actual number of atoms. This can be seen by noticing that the region where the entropy reaches its highest values gets larger as the cooperation number increases.

It is worth remarking that, while the trial state is a tensor product of coherent states and therefore shows no entanglement between matter and the radiation field, the phase diagrams obtained via these variational states is well displayed by the entropy of entanglement calculated through quantum means. In contrast the latter does not dictate the exact quantum phase transitions for finite N; they coincide only in the cooperation-number thermodynamic limit.

From the figures presented, and based on the fact that the coherent QPT and the "real" QPT coincide in the cooperation-number thermodynamic limit, we are able to conclude that there is indeed a resemblance between the QPT of the studied system and the highest values of its entropy of entanglement for a finite number of atoms. This conclusion suggests that there are more than one possible states for which the system can be in at zero temperature; hence, its residual entropy must be different from zero.

Chapter 4

Conclusions

4.1 Two-Level Atoms

From figures presented we conclude that SASc offer a good approximation (with an analytic expression) to the exact quantum solution far from the QPT for low cooperation numbers, but as $j \to \infty$, the interval where the SASc fail to reproduce the correct behavior, becomes smaller.

On the other hand, the SASn provide a better approximation to the quantum solution. This improvement comes with the disadvantage of losing the analytic expression, but still has the advantage over the quantum solution of the computational time. SASn are obtained by numerically minimizing a real function, which is far easier to do (computationally speaking) than numerically diagonalizing the Hamiltonian matrix.

A characterization of the QPT can be made by looking at the entropy of entanglement; that obtained using the quantum solution shows a maximum at the transition, an attribute that SASc and SASn approximations fail to reproduce.

The behavior of the expectation values of the relevant observables of the system $\langle H \rangle$, $\langle J_z \rangle$ and $\langle \nu_\imath \rangle$, is also affected by the QPT, thus allowing us to characterize the QPT by means of its influence over the observables. In general, it can be observed that the four methods (CS, SASc, SASn and quantum solution) converge in the limit $\delta \to 0$, where the case $j \to \infty$ is particularly interesting as the interval around the QPT, where all the approximations are weaker, becomes smaller.

In conclusion, we have shown how the use of variational states to approximate the ground state of a system can be useful to characterize the QPT in a multi-mode Dicke model using the expectation value of the observables relevant to the system and the entropy of entanglement between matter and radiation. We have also introduced a not very commonly used dependence: the cooperation number, showing its influence over the behavior of the system, paying particular attention to the QPT and the accuracy of the used approximations. Some aspects of the multi-mode Dicke model which are not present in the single-mode case were also briefly discussed.

4.2 Three-Level Atoms

For three-level atoms we showed the usefulness of representation theory and the Gelfand-Tsetlin labeling scheme to study systems of matter interacting with radiation in the dipolar approximation, allowing us to easily define the cooperation number and immediately knowing the atomic population of each level in its normal phase.

Coherent states have been used extensively in the study of the interaction of matter with radiation, mainly due to the fact that they provide analytical expressions with which to study the system, as opposed to the numerical results obtained through the diagonalization of the Hamiltonian. It has thus been useful to study how well (or how bad) the coherent states approximate the exact quantum results. When non-symmetric representations are considered, however, the mathematics become much more complicated and obtaining analytic expressions is far from possible.

We see from the studied observables (energy, photon number, half the atomic population between second and first levels, and between third and second levels) that the given definition of the cooperation number (2.18) is consistent with the intuition of an effective number of atoms in the system, mainly by the fact that the area of the normal region (according to the coherent approximation) gets larger as the cooperation number decreases.

The reliability of the coherent approximation was analyzed using the fidelity between the coherent and quantum solutions, along with the real QPT via a drop in the fidelity between quantum neighboring states. In the latter case, traces of the coherent QPT were observed regardless of the fact that this fidelity was calculated using just the quantum solution, a characteristic we attributed, based on the obtained results for two-level systems, to the fact that both solutions coincide in the cooperation-number thermodynamic limit.

An interesting pattern present in the three configurations is that of the increase in the sensitivity of the entropy of entanglement as the cooperation number tends to the actual number of atoms, where by sensitivity. This can be seen by noticing that the region where the entropy reaches its highest values gets larger as the cooperation number increases.

It is worth mentioning that, while the trial state is a tensor product of coherent states and therefore shows no entanglement between matter and the radiation field, the phase diagrams obtained via these variational states is well displayed by the entropy of entanglement calculated through quantum means.

In conclusion, we utilized a coherent approximation to the system's ground state to study its quantum phase transitions, which we used to justify the given definition of cooperation number, showing how this affects the behavior of the relevant observables and the entropy of entanglement near the transitions for all configurations of three-level atoms.

4.3 Main Contributions and Further Work

Even though the formal definition of a QPT requires us to compute the ground state's energy as a function of any desired parameter in order to find its transition values, one the contributions of this work is to show how the QPT in the Dicke model influences the behavior of the entropy of entanglement and the expectation values

of the energy, population difference between levels and number of photons operators, thus characterizing the transition in different, simpler ways.

Equations (3.6), (3.7) and (3.8) provide analytical expressions for the expectation values of the energy, population difference between levels and number of photons operators. These expressions were obtained using symmetry adapted states minimized using coherent states critical points.

We have shown important aspects of the multi-mode Dicke model which are not present in the single-mode case. In figure 3.7 it is displayed how the different modes of radiation (orthogonal in principle) interact through the matter field, analogously as it occurs with different atoms interacting through the radiation field. Additionally, figure 3.16 shows (pictorically) the phase diagrams of the two-mode system, in which it can be observed that any two points in the super-radiant region can be joined by a trajectory that does not cross the normal region, a characteristic that the single-mode system does not have.

In definition (2.18), we generalized the concept of cooperation number given by Dicke, to describe an effective number of multi-level atoms using the labels of the representations of SU(N) present in the Gelfand-Tsetlin labeling scheme. Additionally, an explicit expression of the SU(3) coherent state for an arbitrary representation is given in equation (2.19).

Two aspects of this research are worth studying in more depth, and we suggest them as further work. The first one is to verify the relation between the cooperation number and the area of the normal region of a system with a larger number of three-level atoms; the second one is to study the relation between different representation of SU(3) with same cooperation numbers, the least number of atoms the system needs to have for this to happen is $N = 6$, and the representations are $h = (4, 1, 1)$ and $h = (3, 3, 0)$, both with a cooperation number of $n_c = 3$.

Appendix A

Results for the Λ and V Configurations

A.1 Observables and Fidelities

It is worth mentioning that, due to the heavy numerical minimization, there is some noise present in various graphs of the V configuration, specifically in all those that correspond to the $h = (3, 1, 0)$ and $h = (2, 2, 0)$ representations.

The energy surface (minimized numerically) is shown in figures A.1 and A.2 for the Λ configuration and in figures A.13 and A.14 for the V configuration. In them, the average ground-state's energy of the system is plotted as a function of the corresponding dipolar coupling parameters of each configuration, for all the four possible representations and cooperation numbers (n_c) available for $N = 4$. As in the Ξ configuration, the notion of cooperation number as an effective number of atoms in the system is justified. This means that, as $n_c \longrightarrow 0$, the coupling between matter and radiation must be stronger in order for the system to reach the super-radiant phase.

Figures A.3 and A.4 display the average number of photons in the ground state of the system for the Λ configuration, while figures A.15 and A.16 show it for the V configuration. We observe that both configurations look very similar, rapidly increasing the average number of photons as any of their couplings gets stronger.

The expectation value of the Jz_1 operator, corresponding to the average of half the population difference between the second and first levels, is studied in figures A.5 and A.6 for the Λ configuration, and in figures A.17 and A.18 for the V configuration. On the other hand, the expectation value of the Jz_2 operator, corresponding to the average of half the population difference between the third and second levels, is shown in figures A.7 and A.8 for the Λ configuration, and in figures A.19 and A.20 for the V configuration. From these we see that the Λ and V configurations exhibit the same important feature as the Ξ configuration, namely, the parameters h_1, h_2 and h_3 represent, respectively, the atomic population of the first, second, and third level, in the normal region of the system.

In order to the analyze the reliability of the coherent approximation, we show in figures A.9 to A.12 for the Λ configuration and in figures A.21 to A.24 for the V configuration, the comparison between this and the real quantum solution by means of the fidelity between them $F(Coh, Q)$. Along with the comparison plots, we

display the real QPTs via a drop in the fidelity between neighboring quantum states $F(Q,Q)$. Analogously as for the Ξ configuration, there are mainly two ways in which we can calculate $F(Q,Q)$, and because we decide to show just one of them, lines that are actually continuous in the Fidelity (Q,Q) plots, look dashed.

The Fidelity (Coh,Q) plots show an interesting aspect of the configurations analyzed in this appendix, which is not present for the Ξ configuration. In the normal region $F(Coh,Q) \approx 1$, meaning that both coherent and quantum solutions are nearly identical there, but near the coherent QPT the fidelity starts falling rapidly until it reaches two different values depending on the direction in which we decide to move in the μ_{ij} plane. For both configurations, if we cross the QPT in the direction of a line with a constant μ_{13} (i.e. increasing μ_{23} for the Λ configuration or μ_{12} for the V configuration), the fidelity reaches the value $F(Coh,Q) \approx \frac{1}{2}$, which, as we already discuss in subsection 3.2.1, has to do with a parity symmetry in the Hamiltonian (2.15). However, if we cross the QPT in the direction in which μ_{13} increases, the fidelity reaches the value $F(Coh,Q) \approx 0$, suggesting that the coherent approximation is bad at modeling the super-radiant region when the detuning is large.

Another interesting feature of the system, which is also present for the Ξ configuration, is the trace of the coherent QPT present in the Fidelity (Q,Q) plots. These are more noticeable as the cooperation number increases and are quite a remarkable feature, as there is, in principle, no information about the coherent state approximation in the Fidelity (Q,Q) plots. We conclude that this phenomenon occurs due to the fact that both coherent QPT and real QPT, coincide in the cooperation-number thermodynamic limit (i.e. $n_c \longrightarrow \infty$).

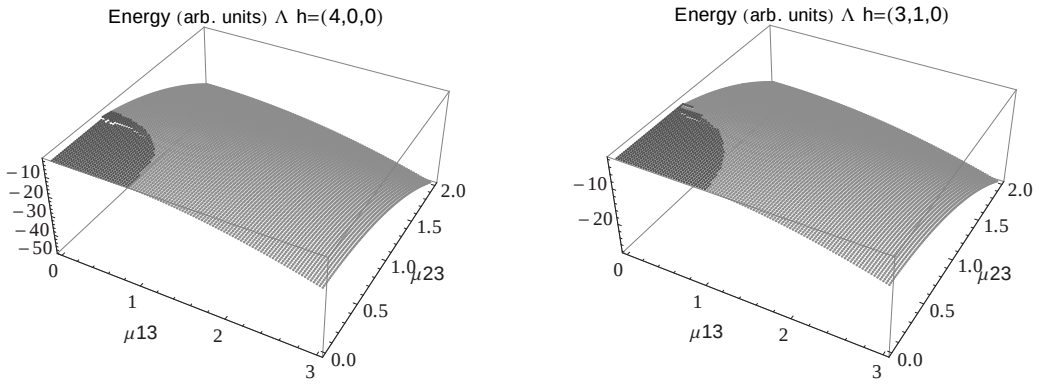

Figure A.1: 3D plot of the energy of the coherent ground state as a function of the coupling parameters μ_{12} and μ_{23}. The dark-gray region represents the normal (sub-radiant) phase of the system. Both figures were obtained using $\omega_1 = 1.\bar{3}$, $\omega_1 = 1.\bar{6}$, $\Omega = 0.5$ and correspond to the Λ configuration. Left: $h = (4,0,0)$, Right: $h = (3,1,0)$. Units are arbitrary but the same for all non-dimensionless quantities ($\hbar = 1$). (Noise in the plots is due to numerical minimization; see text.)

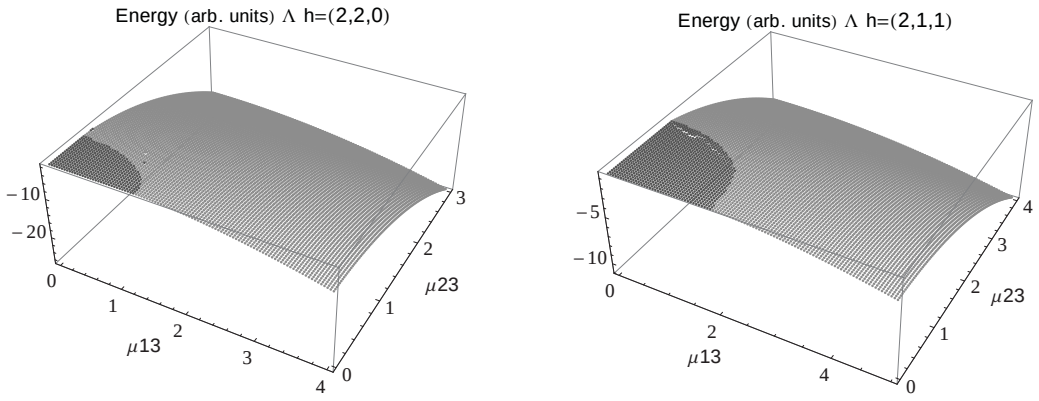

Figure A.2: 3D plot of the energy of the coherent ground state as a function of the coupling parameters μ_{12} and μ_{23}. The dark-gray region represents the normal (sub-radiant) phase of the system. Both figures were obtained using $\omega_1 = 1.\bar{3}$, $\omega_1 = 1.\bar{6}$, $\Omega = 0.5$ and correspond to the Λ configuration. Left: $h = (2, 2, 0)$, Right: $h = (2, 1, 1)$. Units are arbitrary but the same for all non-dimensionless quantities ($\hbar = 1$). (Noise in the plots is due to numerical minimization; see text.)

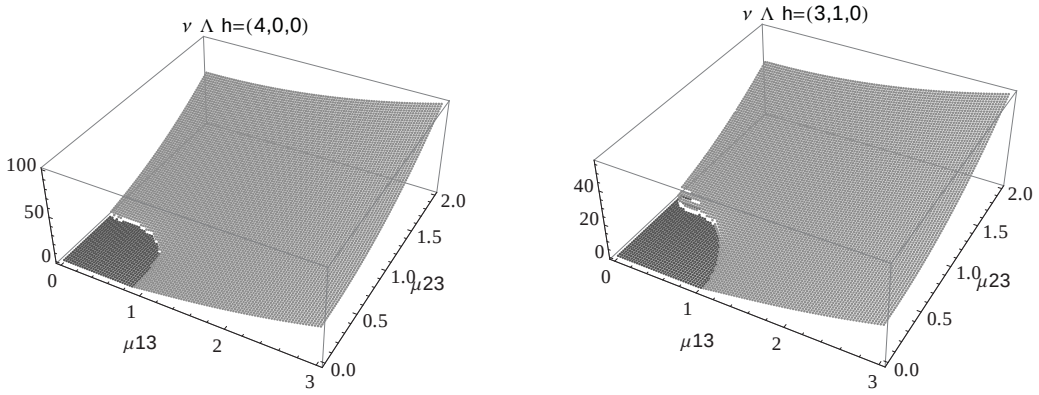

Figure A.3: 3D plot of the average number of photons in the coherent ground state as a function of the coupling parameters μ_{12} and μ_{23}. The dark-gray region represents the normal (sub-radiant) phase of the system. Both figures were obtained using $\omega_1 = 1.\bar{3}$, $\omega_1 = 1.\bar{6}$, $\Omega = 0.5$ and correspond to the Λ configuration. Left: $h = (4, 0, 0)$, Right: $h = (3, 1, 0)$. Units are arbitrary but the same for all non-dimensionless quantities ($\hbar = 1$). (Noise in the plots is due to numerical minimization; see text.)

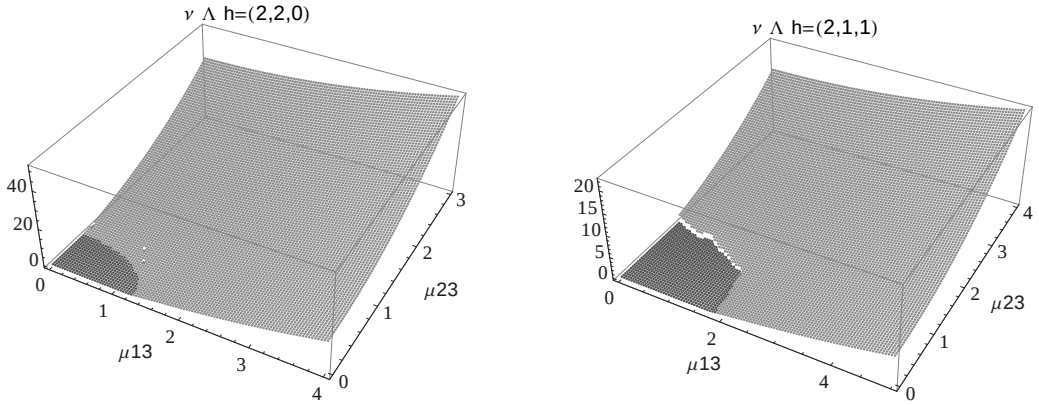

Figure A.4: 3D plot of the average number of photons in the coherent ground state as a function of the coupling parameters μ_{12} and μ_{23}. The dark-gray region represents the normal (sub-radiant) phase of the system. Both figures were obtained using $\omega_1 = 1.\bar{3}$, $\omega_1 = 1.\bar{6}$, $\Omega = 0.5$ and correspond to the Λ configuration. Left: $h = (2, 2, 0)$, Right: $h = (2, 1, 1)$. Units are arbitrary but the same for all non-dimensionless quantities ($\hbar = 1$). (Noise in the plots is due to numerical minimization; see text.)

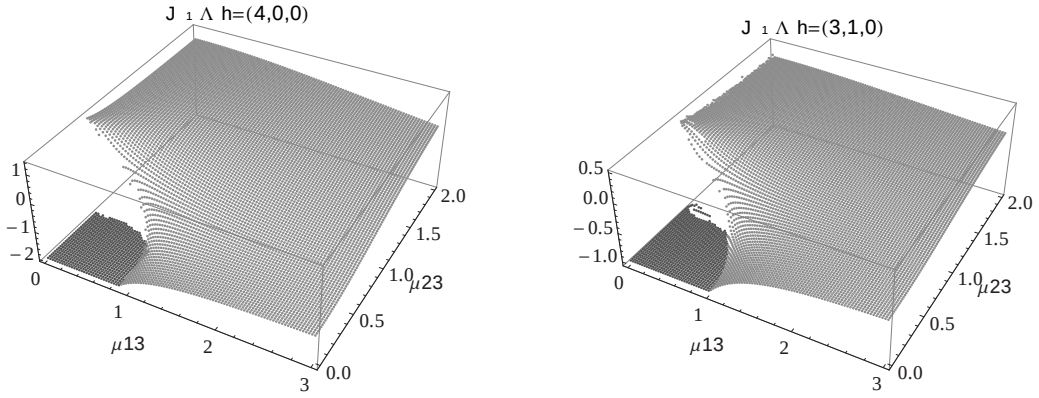

Figure A.5: 3D plot of the expectation value of the Jz_1 operator (half the population difference between the second and first levels) in the coherent ground state as a function of the coupling parameters μ_{12} and μ_{23}. The dark-gray region represents the normal (sub-radiant) phase of the system. Both figures were obtained using $\omega_1 = 1.\bar{3}$, $\omega_1 = 1.\bar{6}$, $\Omega = 0.5$ and correspond to the Λ configuration. Left: $h = (4, 0, 0)$, Right: $h = (3, 1, 0)$. Units are arbitrary but the same for all non-dimensionless quantities ($\hbar = 1$). (Noise in the plots is due to numerical minimization; see text.)

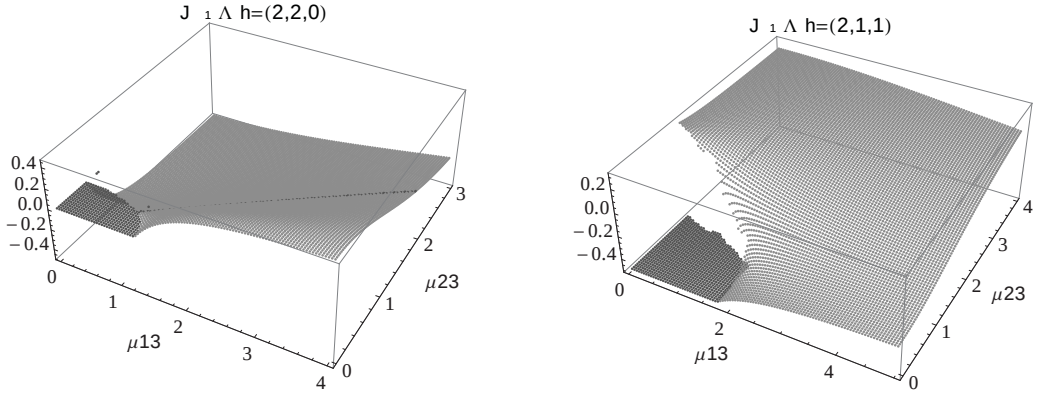

Figure A.6: 3D plot of the expectation value of the Jz_1 operator (half the population difference between the second and first levels) in the coherent ground state as a function of the coupling parameters μ_{12} and μ_{23}. The dark-gray region represents the normal (sub-radiant) phase of the system. Both figures were obtained using $\omega_1 = 1.\bar{3}$, $\omega_1 = 1.\bar{6}$, $\Omega = 0.5$ and correspond to the Λ configuration. Left: $h = (2, 2, 0)$, Right: $h = (2, 1, 1)$. Units are arbitrary but the same for all non-dimensionless quantities ($\hbar = 1$). (Noise in the plots is due to numerical minimization; see text.)

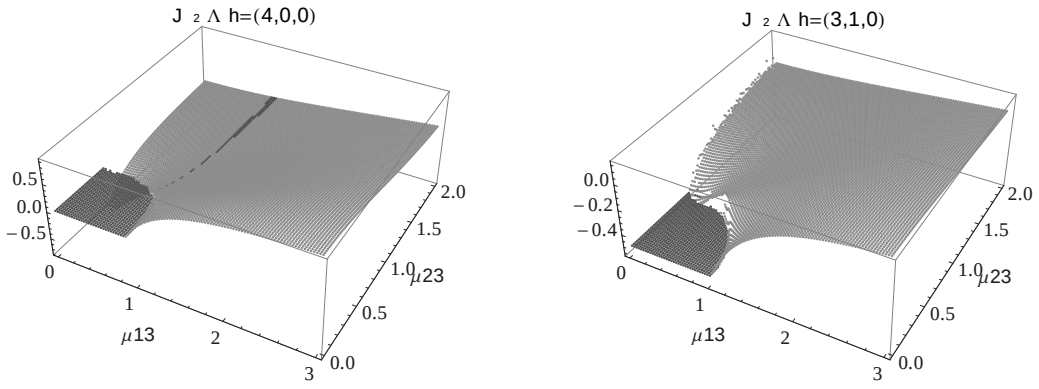

Figure A.7: 3D plot of the expectation value of the Jz_2 operator (half the population difference between the third and second levels) in the coherent ground state as a function of the coupling parameters μ_{12} and μ_{23}. The dark-gray region represents the normal (sub-radiant) phase of the system. Both figures were obtained using $\omega_1 = 1.\bar{3}$, $\omega_1 = 1.\bar{6}$, $\Omega = 0.5$ and correspond to the Λ configuration. Left: $h = (4, 0, 0)$, Right: $h = (3, 1, 0)$. Units are arbitrary but the same for all non-dimensionless quantities ($\hbar = 1$). (Noise in the plots is due to numerical minimization; see text.)

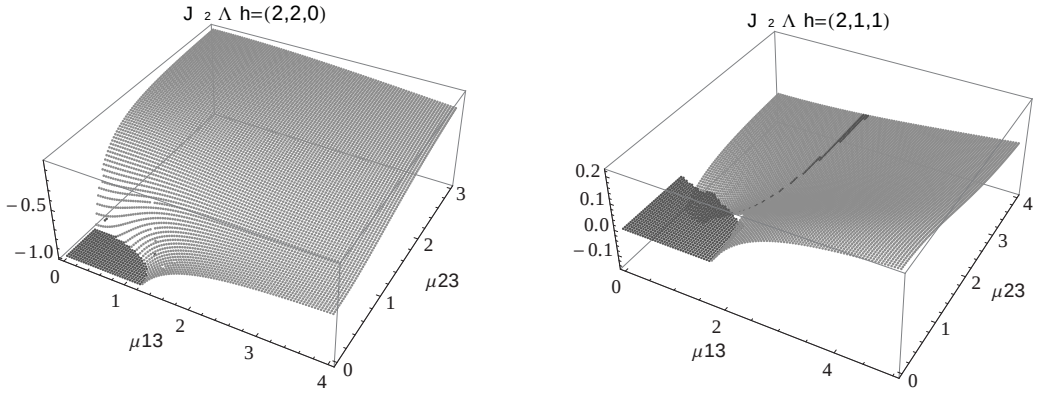

Figure A.8: 3D plot of the expectation value of the Jz_2 operator (half the population difference between the third and second levels) in the coherent ground state as a function of the coupling parameters μ_{12} and μ_{23}. The dark-gray region represents the normal (sub-radiant) phase of the system. Both figures were obtained using $\omega_1 = 1.\bar{3}$, $\omega_1 = 1.\bar{6}$, $\Omega = 0.5$ and correspond to the Λ configuration. Left: $h = (2, 2, 0)$, Right: $h = (2, 1, 1)$. Units are arbitrary but the same for all non-dimensionless quantities ($\hbar = 1$). (Noise in the plots is due to numerical minimization; see text.)

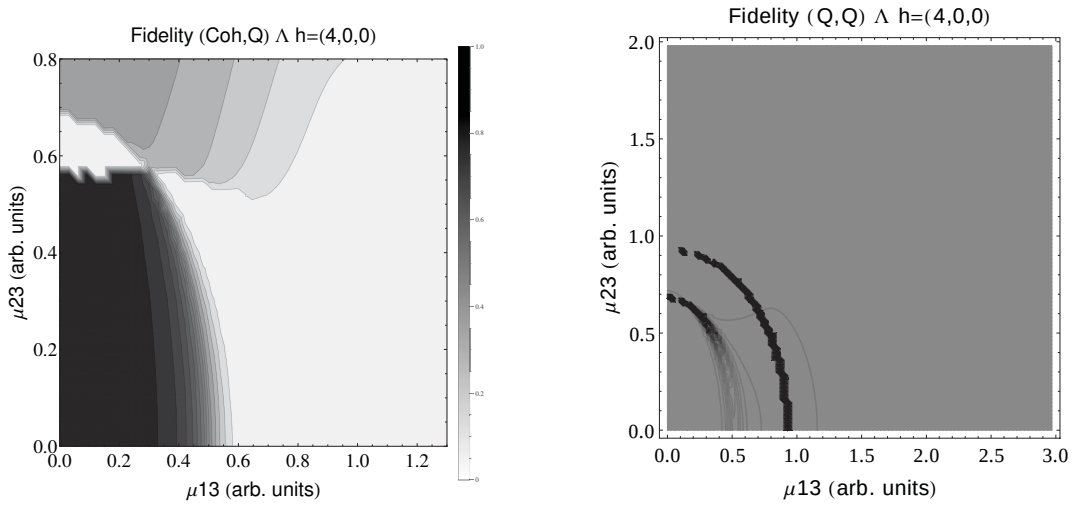

Figure A.9: Left: Contour plot of the fidelity between coherent states and quantum solution as a function of the coupling parameters μ_{12} and μ_{23}, values range between 0 (white) and 1 (black). Right: Contour plot of the fidelity between neighboring quantum states as a function of the coupling parameters μ_{12} and μ_{23}, black dots represent a drop in the fidelity below 1. Both figures were obtained using $\omega_1 = 1.\bar{3}$, $\omega_1 = 1.\bar{6}$, $\Omega = 0.5$ and correspond to the Λ configuration in the $h = (4, 0, 0)$ representation. Units are arbitrary but the same for all non-dimensionless quantities ($\hbar = 1$). (Noise in the plots is due to numerical minimization; see text.)

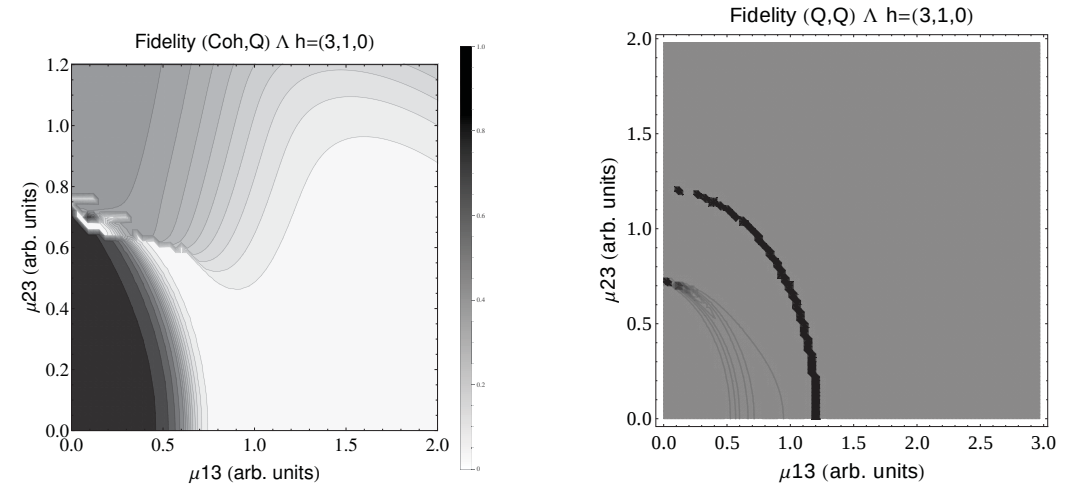

Figure A.10: Left: Contour plot of the fidelity between coherent states and quantum solution as a function of the coupling parameters μ_{12} and μ_{23}, values range between 0 (white) and 1 (black). Right: Contour plot of the fidelity between neighboring quantum states as a function of the coupling parameters μ_{12} and μ_{23}, black dots represent a drop in the fidelity below 1. Both figures were obtained using $\omega_1 = 1.\bar{3}$, $\omega_1 = 1.\bar{6}$, $\Omega = 0.5$ and correspond to the Λ configuration in the $h = (3, 1, 0)$ representation. Units are arbitrary but the same for all non-dimensionless quantities ($\hbar = 1$). (Noise in the plots is due to numerical minimization; see text.)

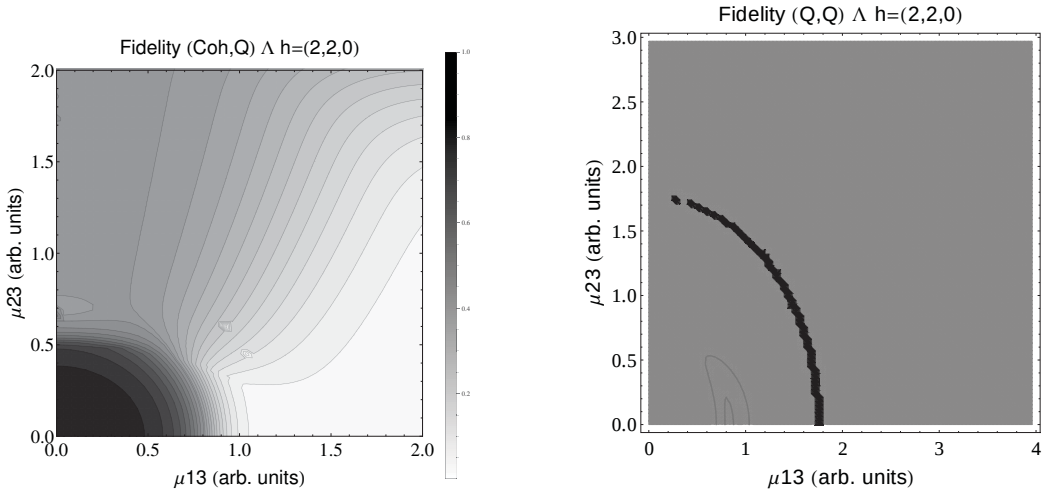

Figure A.11: Left: Contour plot of the fidelity between coherent states and quantum solution as a function of the coupling parameters μ_{12} and μ_{23}, values range between 0 (white) and 1 (black). Right: Contour plot of the fidelity between neighboring quantum states as a function of the coupling parameters μ_{12} and μ_{23}, black dots represent a drop in the fidelity below 1. Both figures were obtained using $\omega_1 = 1.\bar{3}$, $\omega_1 = 1.\bar{6}$, $\Omega = 0.5$ and correspond to the Λ configuration in the $h = (2, 2, 0)$ representation. Units are arbitrary but the same for all non-dimensionless quantities ($\hbar = 1$). (Noise in the plots is due to numerical minimization; see text.)

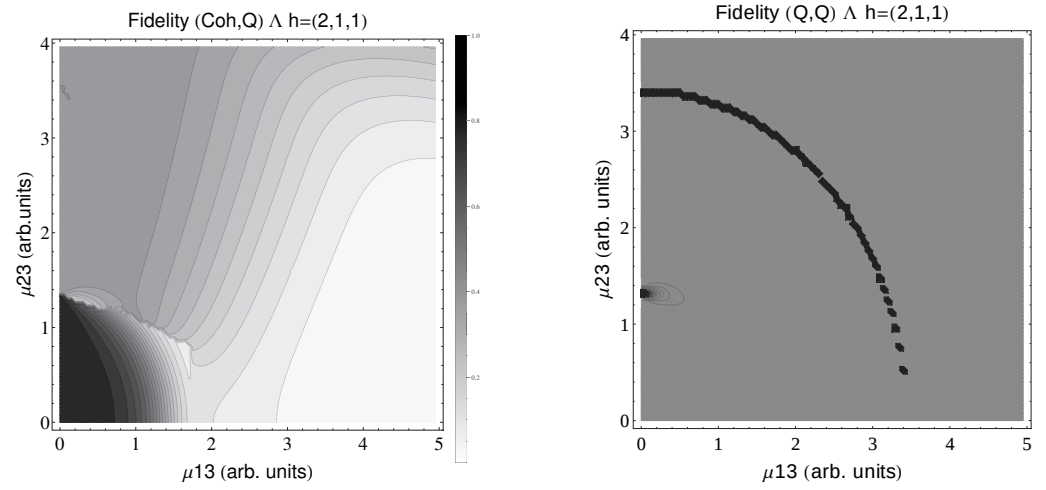

Figure A.12: Left: Contour plot of the fidelity between coherent states and quantum solution as a function of the coupling parameters μ_{12} and μ_{23}, values range between 0 (white) and 1 (black). Right: Contour plot of the fidelity between neighboring quantum states as a function of the coupling parameters μ_{12} and μ_{23}, black dots represent a drop in the fidelity below 1. Both figures were obtained using $\omega_1 = 1.\bar{3}$, $\omega_1 = 1.\bar{6}$, $\Omega = 0.5$ and correspond to the Λ configuration in the $h = (2, 1, 1)$ representation. Units are arbitrary but the same for all non-dimensionless quantities ($\hbar = 1$). (Noise in the plots is due to numerical minimization; see text.)

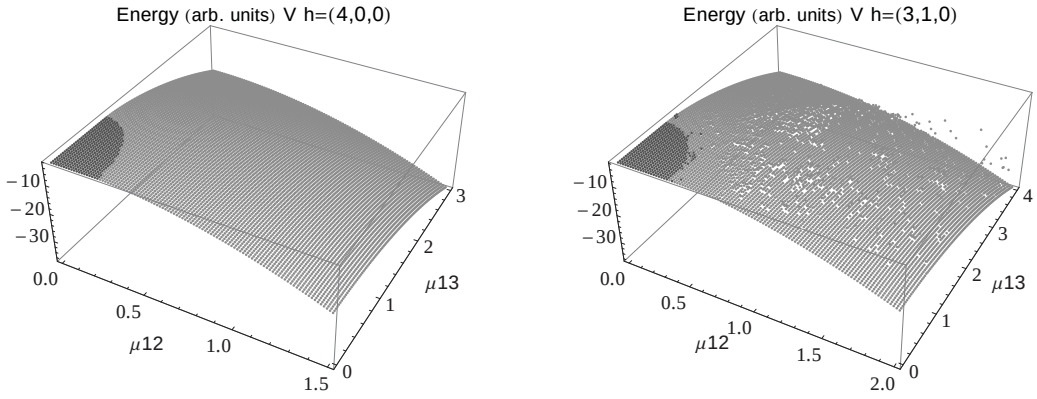

Figure A.13: 3D plot of the energy of the coherent ground state as a function of the coupling parameters μ_{12} and μ_{23}. The dark-gray region represents the normal (sub-radiant) phase of the system. Both figures were obtained using $\omega_1 = 1.\bar{3}$, $\omega_1 = 1.\bar{6}$, $\Omega = 0.5$ and correspond to the V configuration. Left: $h = (4, 0, 0)$, Right: $h = (3, 1, 0)$. Units are arbitrary but the same for all non-dimensionless quantities ($\hbar = 1$). (Noise in the plots is due to numerical minimization; see text.)

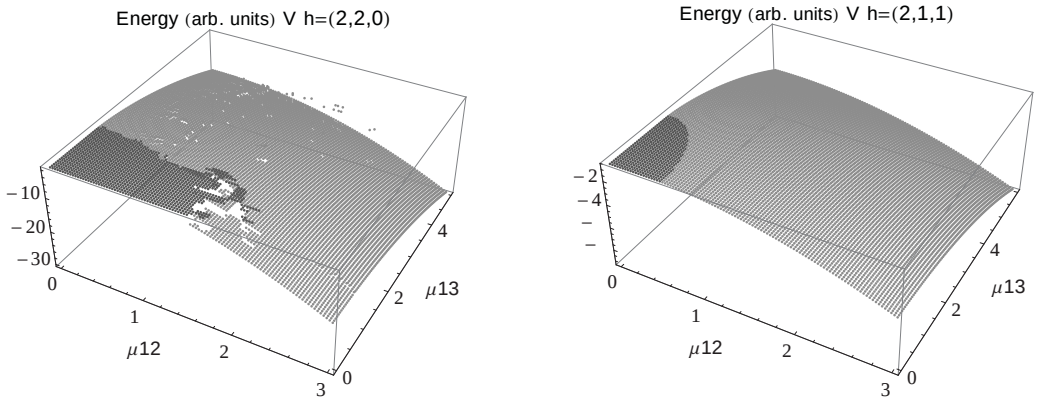

Figure A.14: 3D plot of the energy of the coherent ground state as a function of the coupling parameters μ_{12} and μ_{23}. The dark-gray region represents the normal (sub-radiant) phase of the system. Both figures were obtained using $\omega_1 = 1.\bar{3}$, $\omega_1 = 1.\bar{6}$, $\Omega = 0.5$ and correspond to the V configuration. Left: $h = (2, 2, 0)$, Right: $h = (2, 1, 1)$. Units are arbitrary but the same for all non-dimensionless quantities ($\hbar = 1$). (Noise in the plots is due to numerical minimization; see text.)

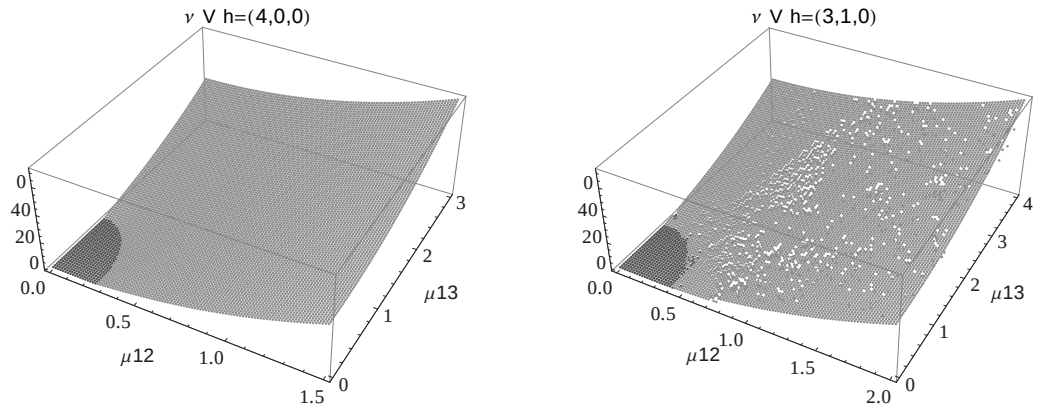

Figure A.15: 3D plot of the average number of photons in the coherent ground state as a function of the coupling parameters μ_{12} and μ_{23}. The dark-gray region represents the normal (sub-radiant) phase of the system. Both figures were obtained using $\omega_1 = 1.\bar{3}$, $\omega_1 = 1.\bar{6}$, $\Omega = 0.5$ and correspond to the V configuration. Left: $h = (4, 0, 0)$, Right: $h = (3, 1, 0)$. Units are arbitrary but the same for all non-dimensionless quantities ($\hbar = 1$). (Noise in the plots is due to numerical minimization; see text.)

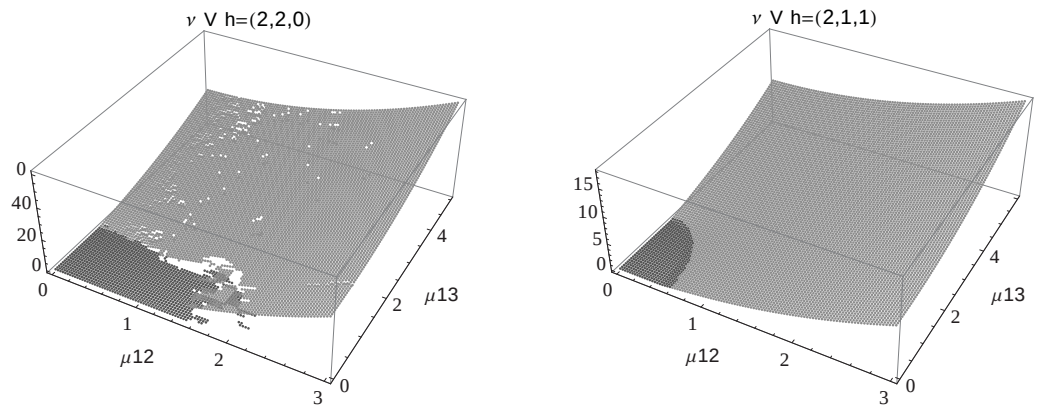

Figure A.16: 3D plot of the average number of photons in the coherent ground state as a function of the coupling parameters μ_{12} and μ_{23}. The dark-gray region represents the normal (sub-radiant) phase of the system. Both figures were obtained using $\omega_1 = 1.\bar{3}$, $\omega_1 = 1.\bar{6}$, $\Omega = 0.5$ and correspond to the V configuration. Left: $h = (2, 2, 0)$, Right: $h = (2, 1, 1)$. Units are arbitrary but the same for all non-dimensionless quantities ($\hbar = 1$). (Noise in the plots is due to numerical minimization; see text.)

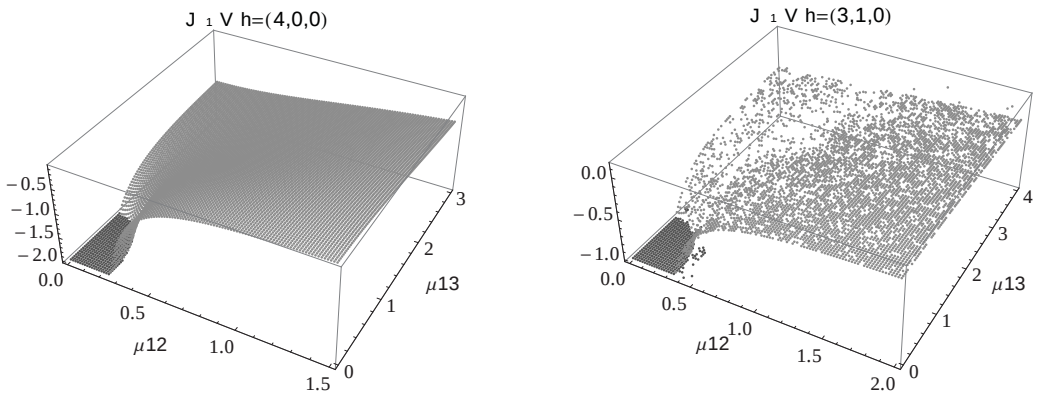

Figure A.17: 3D plot of the expectation value of the Jz_1 operator (half the population difference between the second and first levels) in the coherent ground state as a function of the coupling parameters μ_{12} and μ_{23}. The dark-gray region represents the normal (sub-radiant) phase of the system. Both figures were obtained using $\omega_1 = 1.\bar{3}$, $\omega_1 = 1.\bar{6}$, $\Omega = 0.5$ and correspond to the V configuration. Left: $h = (4, 0, 0)$, Right: $h = (3, 1, 0)$. Units are arbitrary but the same for all non-dimensionless quantities ($\hbar = 1$). (Noise in the plots is due to numerical minimization; see text.)

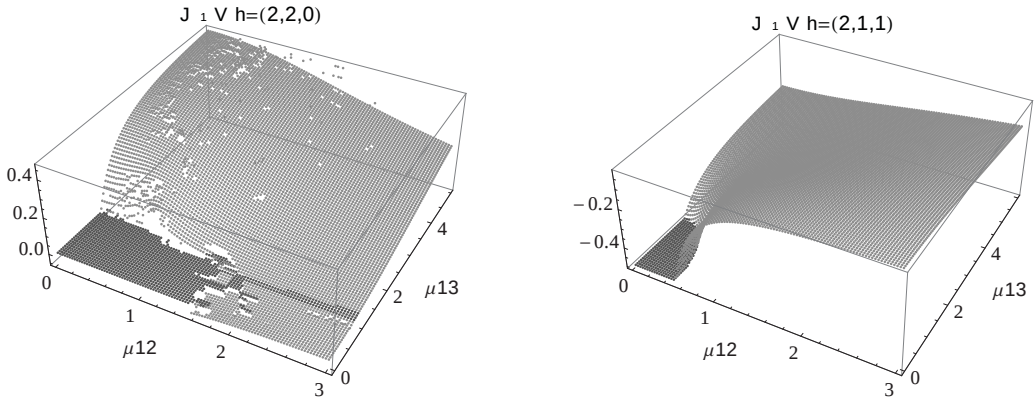

Figure A.18: 3D plot of the expectation value of the Jz_1 operator (half the population difference between the second and first levels) in the coherent ground state as a function of the coupling parameters μ_{12} and μ_{23}. The dark-gray region represents the normal (sub-radiant) phase of the system. Both figures were obtained using $\omega_1 = 1.\bar{3}$, $\omega_1 = 1.\bar{6}$, $\Omega = 0.5$ and correspond to the V configuration. Left: $h = (2, 2, 0)$, Right: $h = (2, 1, 1)$. Units are arbitrary but the same for all non-dimensionless quantities ($\hbar = 1$). (Noise in the plots is due to numerical minimization; see text.)

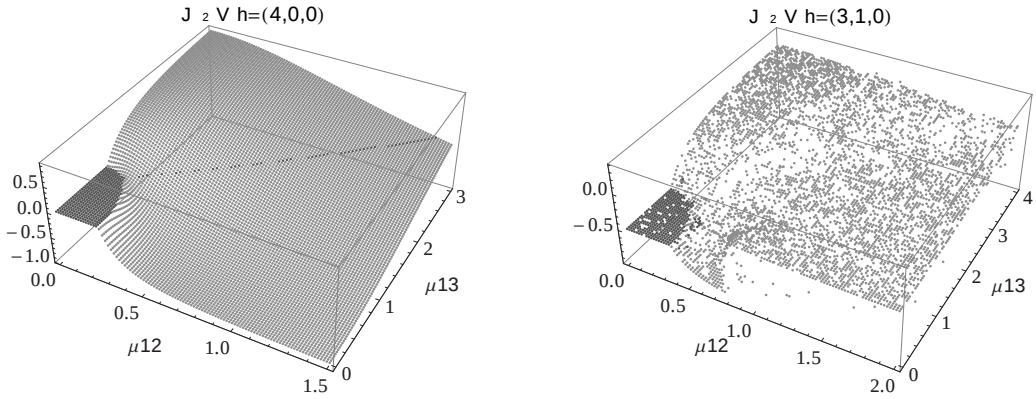

Figure A.19: 3D plot of the expectation value of the Jz_2 operator (half the population difference between the third and second levels) in the coherent ground state as a function of the coupling parameters μ_{12} and μ_{23}. The dark-gray region represents the normal (sub-radiant) phase of the system. Both figures were obtained using $\omega_1 = 1.\bar{3}$, $\omega_1 = 1.\bar{6}$, $\Omega = 0.5$ and correspond to the V configuration. Left: $h = (4, 0, 0)$, Right: $h = (3, 1, 0)$. Units are arbitrary but the same for all non-dimensionless quantities ($\hbar = 1$). (Noise in the plots is due to numerical minimization; see text.)

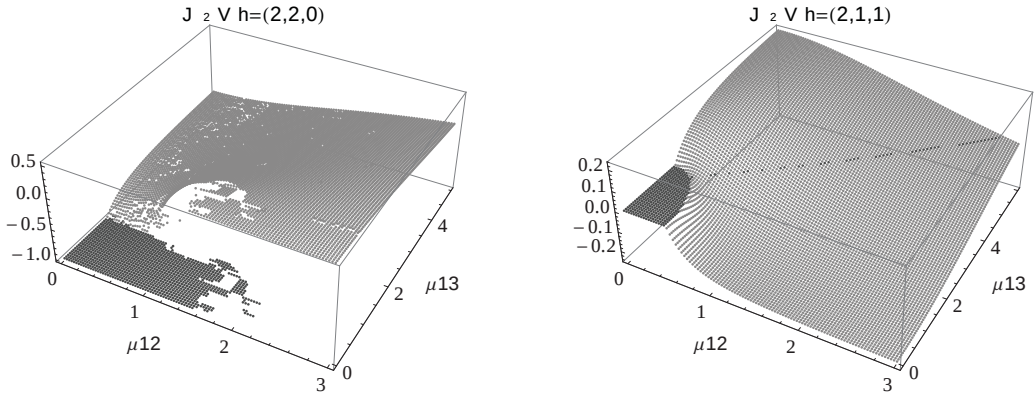

Figure A.20: 3D plot of the expectation value of the Jz_2 operator (half the population difference between the third and second levels) in the coherent ground state as a function of the coupling parameters μ_{12} and μ_{23}. The dark-gray region represents the normal (sub-radiant) phase of the system. Both figures were obtained using $\omega_1 = 1.\bar{3}$, $\omega_1 = 1.\bar{6}$, $\Omega = 0.5$ and correspond to the V configuration. Left: $h = (2, 2, 0)$, Right: $h = (2, 1, 1)$. Units are arbitrary but the same for all non-dimensionless quantities ($\hbar = 1$). (Noise in the plots is due to numerical minimization; see text.)

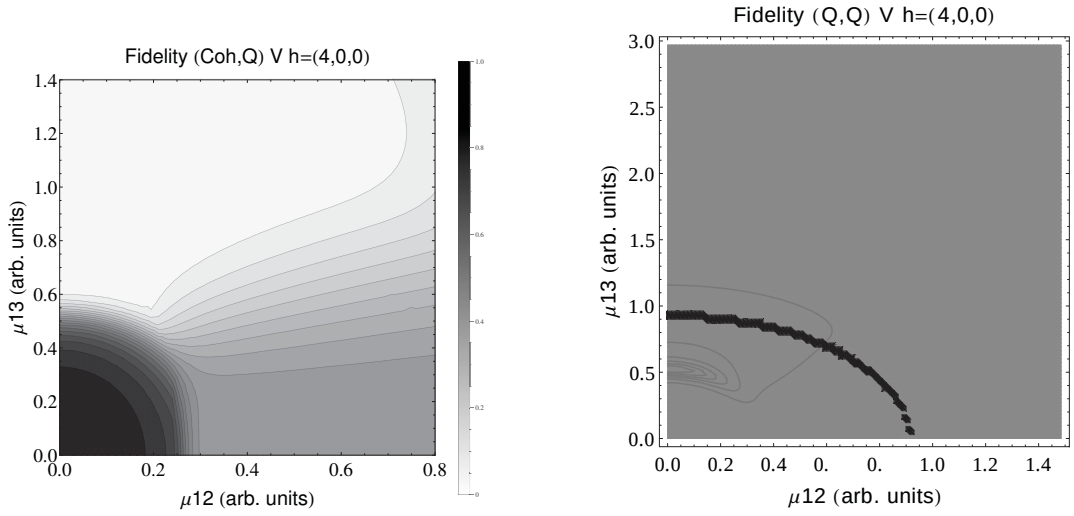

Figure A.21: Left: Contour plot of the fidelity between coherent states and quantum solution as a function of the coupling parameters μ_{12} and μ_{23}, values range between 0 (white) and 1 (black). Right: Contour plot of the fidelity between neighboring quantum states as a function of the coupling parameters μ_{12} and μ_{23}, black dots represent a drop in the fidelity below 1. Both figures were obtained using $\omega_1 = 1.\bar{3}$, $\omega_1 = 1.\bar{6}$, $\Omega = 0.5$ and correspond to the V configuration in the $h = (4, 0, 0)$ representation. Units are arbitrary but the same for all non-dimensionless quantities ($\hbar = 1$). (Noise in the plots is due to numerical minimization; see text.)

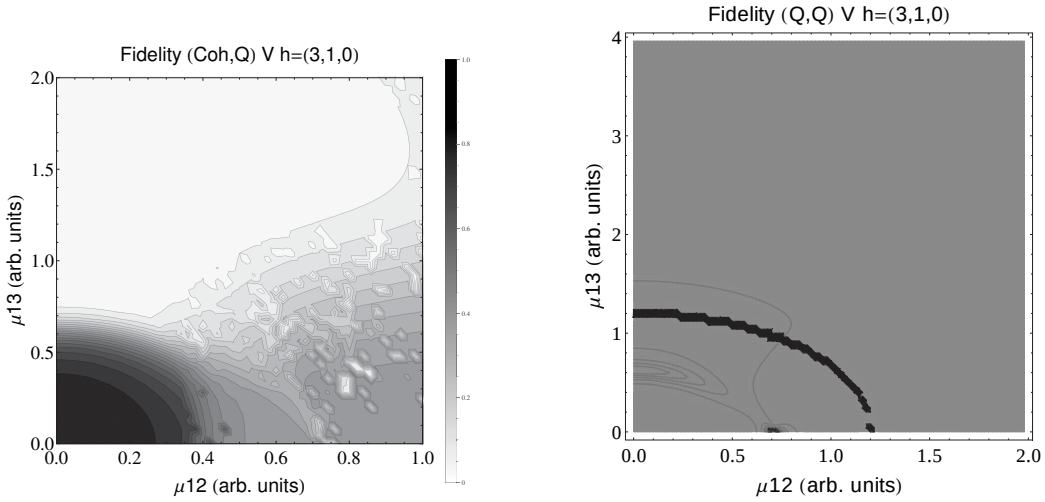

Figure A.22: Left: Contour plot of the fidelity between coherent states and quantum solution as a function of the coupling parameters μ_{12} and μ_{23}, values range between 0 (white) and 1 (black). Right: Contour plot of the fidelity between neighboring quantum states as a function of the coupling parameters μ_{12} and μ_{23}, black dots represent a drop in the fidelity below 1. Both figures were obtained using $\omega_1 = 1.\bar{3}$, $\omega_1 = 1.\bar{6}$, $\Omega = 0.5$ and correspond to the V configuration in the $h = (3, 1, 0)$ representation. Units are arbitrary but the same for all non-dimensionless quantities ($\hbar = 1$). (Noise in the plots is due to numerical minimization; see text.)

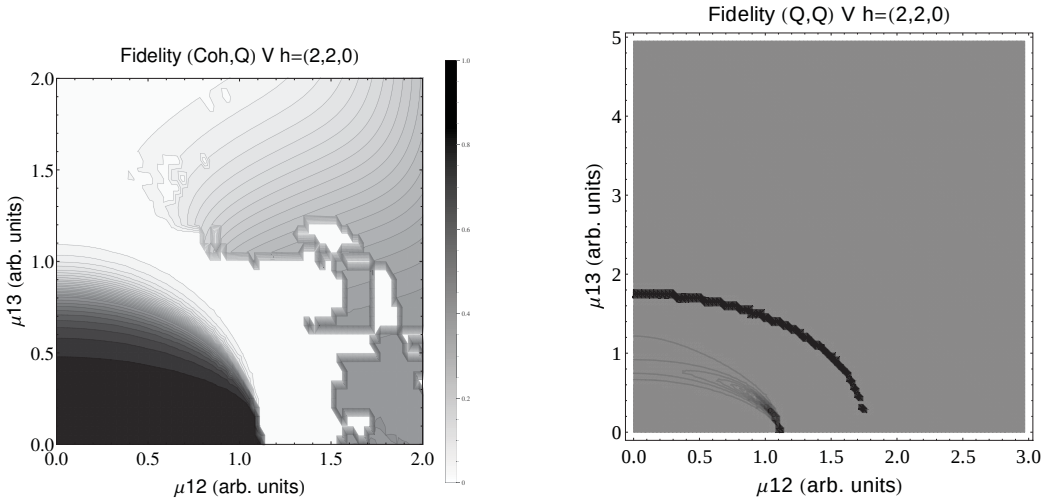

Figure A.23: Left: Contour plot of the fidelity between coherent states and quantum solution as a function of the coupling parameters μ_{12} and μ_{23}, values range between 0 (white) and 1 (black). Right: Contour plot of the fidelity between neighboring quantum states as a function of the coupling parameters μ_{12} and μ_{23}, black dots represent a drop in the fidelity below 1. Both figures were obtained using $\omega_1 = 1.\bar{3}$, $\omega_1 = 1.\bar{6}$, $\Omega = 0.5$ and correspond to the V configuration in the $h = (2, 2, 0)$ representation. Units are arbitrary but the same for all non-dimensionless quantities ($\hbar = 1$). (Noise in the plots is due to numerical minimization; see text.)

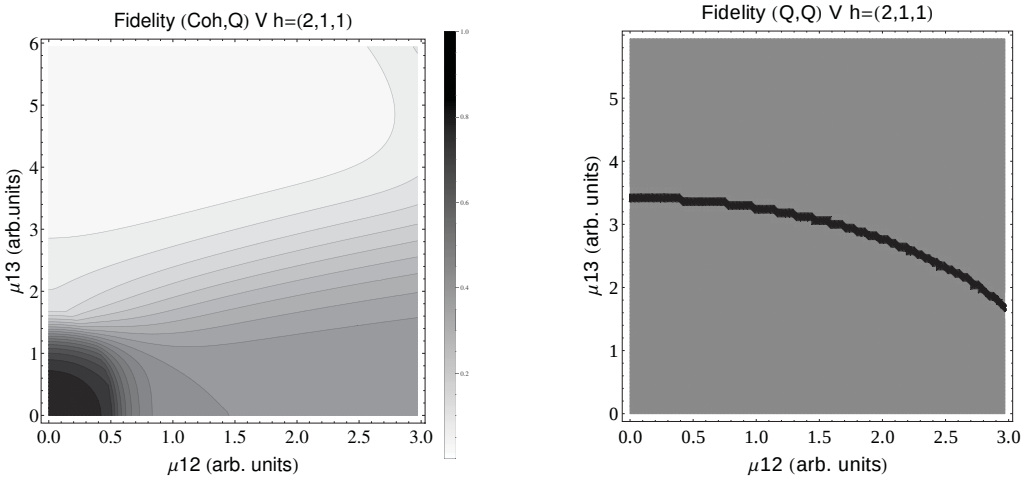

Figure A.24: Left: Contour plot of the fidelity between coherent states and quantum solution as a function of the coupling parameters μ_{12} and μ_{23}, values range between 0 (white) and 1 (black). Right: Contour plot of the fidelity between neighboring quantum states as a function of the coupling parameters μ_{12} and μ_{23}, black dots represent a drop in the fidelity below 1. Both figures were obtained using $\omega_1 = 1.\bar{3}$, $\omega_1 = 1.\bar{6}$, $\Omega = 0.5$ and correspond to the V configuration in the $h = (2, 1, 1)$ representation. Units are arbitrary but the same for all non-dimensionless quantities ($\hbar = 1$). (Noise in the plots is due to numerical minimization; see text.)

A.2 Entropy of Entanglement

The results for atoms in the Λ configuration are presented in figures A.25–A.28 for all four possible cooperation numbers. The first two graphics (from left to right) show the entropy of entanglement. In them, the region where the entropy reaches its highest values ($S_\varepsilon > 1.01$) is shown in dark gray As with the Ξ configuration, it is worth noticing that this region gets larger as the cooperation number increases.

The third graphic shows a contour plot of the fidelity between neighboring coherent states. In this, the region where the fidelity drops ($F < 0.97$ is emphasized although fidelity drops to values near zero) is shown in dark gray. Irregularities appear due to numerical errors in the energy surface's minimization process near the transition.

Finally, we present the results for atoms in the V configuration in figures A.29–A.32, for all four possible cooperation numbers. The first two graphics (from left to right) show the entropy of entanglement, in them, the region where the entropy reaches its highest values ($S_\varepsilon > 1.03$) is shown in dark gray. As in the previous configurations, it's worth noting that this region gets larger as the cooperation number increases.

The third graphic shows a contour plot of the fidelity between neighboring coherent states, in this, the region where the fidelity drops ($F < 0.97$ is emphasized although fidelity drops to values near zero) is shown in dark gray. Irregularities appear due to numerical errors in the energy surface's minimization process near the transition.

In the Λ and V configurations there is evidence of only two phases in the phase space of its ground state at zero temperature, the normal and collective regions, and these are well determined by the entropy of entanglement.

As in the Ξ configuration, the sensitivity of the entropy of entanglement increases as the cooperation number tends to the actual number of atoms. This can be seen by noticing that the region where the entropy reaches its highest values gets larger as the cooperation number increases.

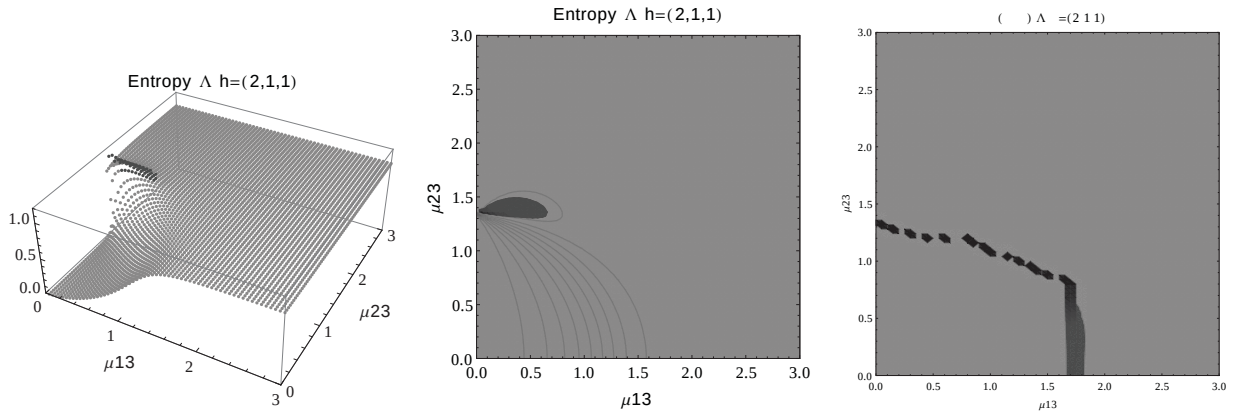

Figure A.25: (**Left**) 3D plot of the entropy of entanglement as a function of the coupling parameters μ_{13} and μ_{23}, the maximum value of the entropy is $S_\varepsilon = 1.15$ and the region where S_ε >1.01 is shown in dark gray (**Center**) Contour plot of the entropy of entanglement as a function of the coupling parameters μ_{13} and μ_{23}, the region where S_ε >1.01 is shown in dark gray (**Right**) Fidelity between neighboring coherent states as a function of the coupling parameters μ_{13} and μ_{23}, dark gray region shows the fidelity's minimum (i.e., the phase transition). All figures use $\omega_1 = 1.\bar{3}$, $\omega_2 = 1.\bar{6}$, $\Omega = 0.5$ and correspond to the Λ configuration and the $h = (2, 1, 1)$ representation.

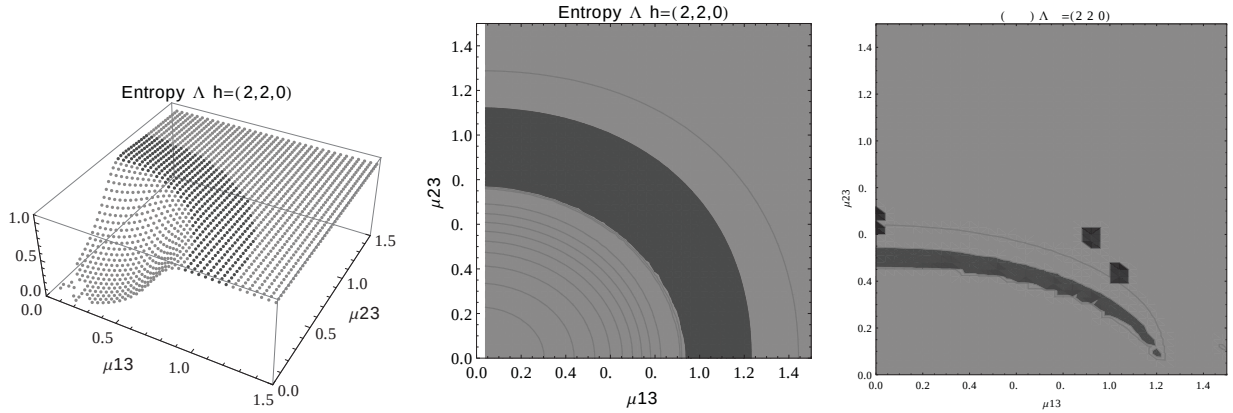

Figure A.26: (**Left**) 3D plot of the entropy of entanglement as a function of the coupling parameters μ_{13} and μ_{23}, the maximum value of the entropy is $S_\varepsilon = 1.03$ and the region where S_ε >1.01 is shown in dark gray (**Center**) Contour plot of the entropy of entanglement as a function of the coupling parameters μ_{13} and μ_{23}, the region where S_ε >1.01 is shown in dark gray (**Right**) Fidelity between neighboring coherent states as a function of the coupling parameters μ_{13} and μ_{23}, dark gray region shows the fidelity's minimum (i.e., the phase transition). All figures use $\omega_1 = 1.\bar{3}$, $\omega_2 = 1.\bar{6}$, $\Omega = 0.5$ and correspond to the Λ configuration and the $h = (2, 2, 0)$ representation.

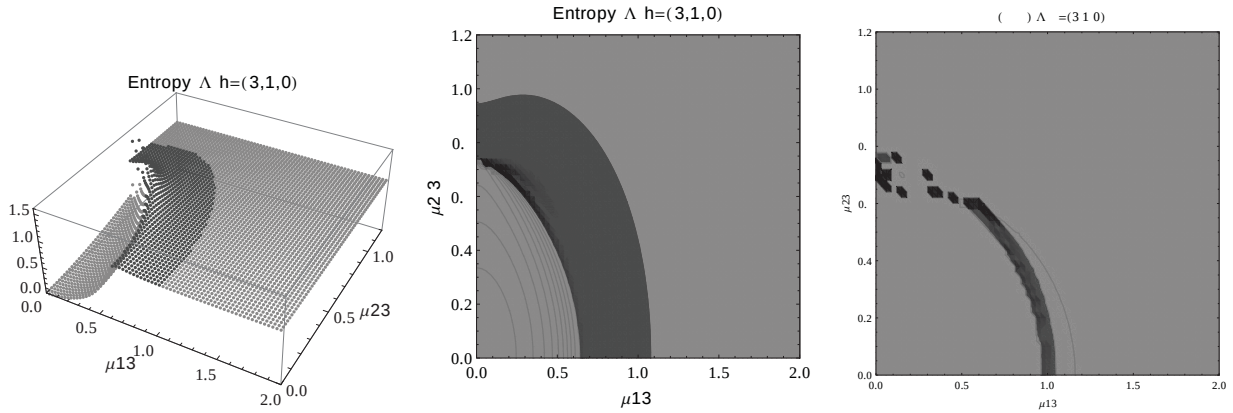

Figure A.27: (**Left**) 3D plot of the entropy of entanglement as a function of the coupling parameters μ_{13} and μ_{23}, the maximum value of the entropy is $S_\varepsilon = 1.59$ and the region where S_ε >1.01 is shown in dark gray (**Center**) Contour plot of the entropy of entanglement as a function of the coupling parameters μ_{13} and μ_{23}, the region where S_ε >1.01 is shown in dark gray (**Right**) Fidelity between neighboring coherent states as a function of the coupling parameters μ_{13} and μ_{23}, dark gray region shows the fidelity's minimum (i.e., the phase transition). All figures use $\omega_1 = 1.\bar{3}$, $\omega_2 = 1.\bar{6}$, $\Omega = 0.5$ and correspond to the Λ configuration and the $h = (3, 1, 0)$ representation.

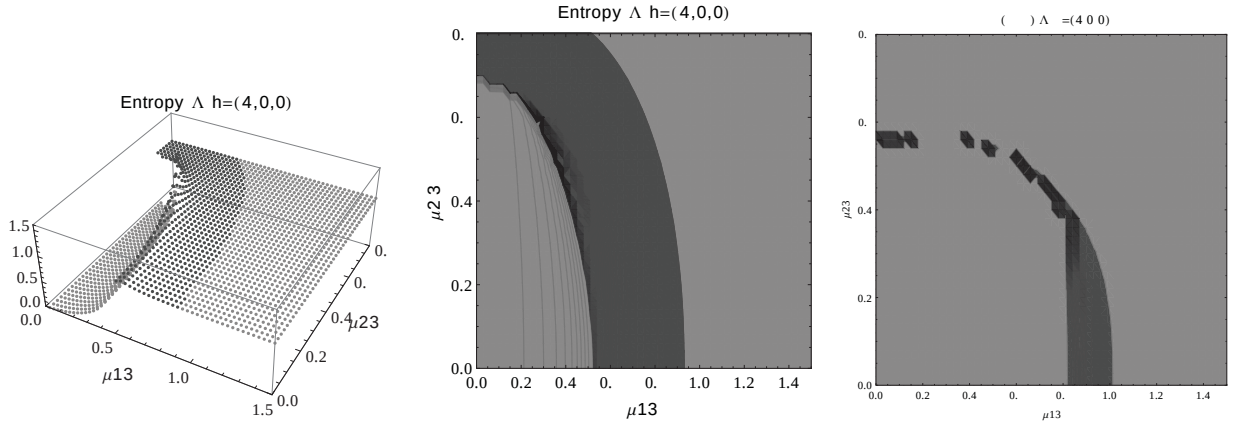

Figure A.28: (**Left**) 3D plot of the entropy of entanglement as a function of the coupling parameters μ_{13} and μ_{23}, the maximum value of the entropy is $S_\varepsilon = 1.55$ and the region where S_ε >1.01 is shown in dark gray (**Center**) Contour plot of the entropy of entanglement as a function of the coupling parameters μ_{13} and μ_{23}, the region where S_ε >1.01 is shown in dark gray (**Right**) Fidelity between neighboring coherent states as a function of the coupling parameters μ_{13} and μ_{23}, dark gray region shows the fidelity's minimum (i.e., the phase transition). All figures use $\omega_1 = 1.\bar{3}$, $\omega_2 = 1.\bar{6}$, $\Omega = 0.5$ and correspond to the Λ configuration and the $h = (4, 0, 0)$ representation.

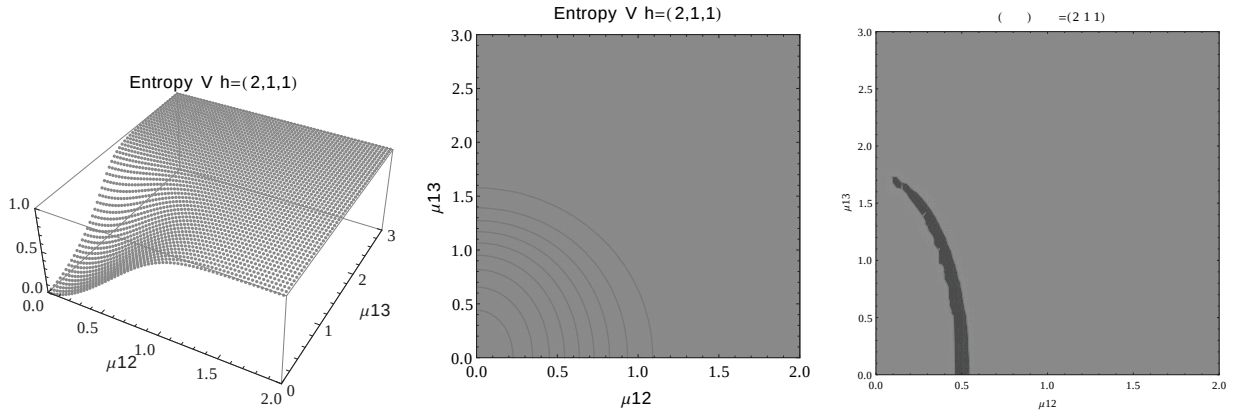

Figure A.29: (**Left**) 3D plot of the entropy of entanglement as a function of the coupling parameters μ_{12} and μ_{13}, the maximum value of the entropy is $S_\varepsilon = 1$. (**Center**) Contour plot of the entropy of entanglement as a function of the coupling parameters μ_{12} and μ_{13}. (**Right**) Fidelity between neighboring coherent states as a function of the coupling parameters μ_{12} and μ_{13}, dark gray region shows the fidelity's minimum (i.e., the phase transition). All figures use $\omega_1 = 1.\bar{3}$, $\omega_2 = 1.\bar{6}$, $\Omega = 0.5$ and correspond to the V configuration and the $h = (2, 1, 1)$ representation.

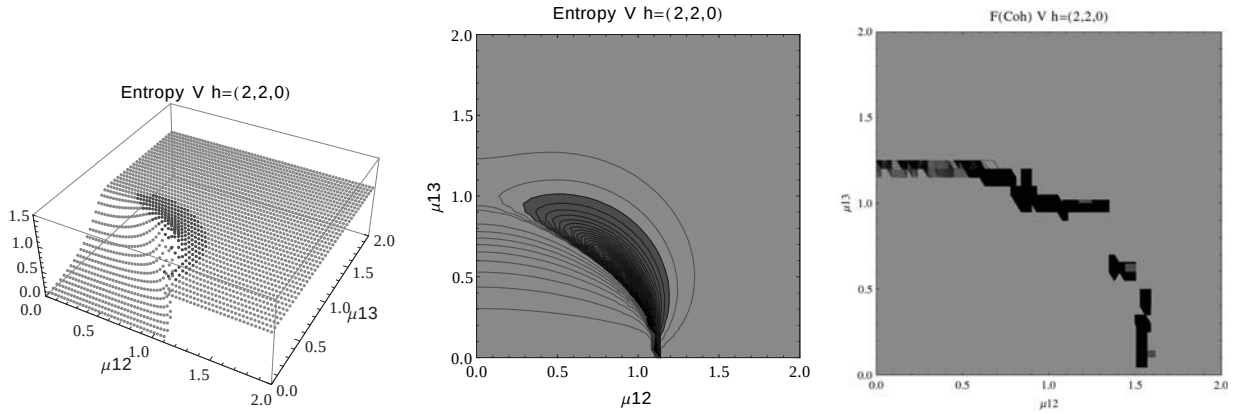

Figure A.30: (**Left**) 3D plot of the entropy of entanglement as a function of the coupling parameters μ_{12} and μ_{13}, the maximum value of the entropy is $S_\varepsilon = 1.55$ and the region where $S_\varepsilon > 1.03$ is shown in dark gray (**Center**) Contour plot of the entropy of entanglement as a function of the coupling parameters μ_{12} and μ_{13}, the region where $S_\varepsilon > 1.03$ is shown in dark gray (**Right**) Fidelity between neighboring coherent states as a function of the coupling parameters μ_{12} and μ_{13}, dark gray region shows the fidelity's minimum (i.e., the phase transition). All figures use $\omega_1 = 1.\bar{3}$, $\omega_2 = 1.\bar{6}$, $\Omega = 0.5$ and correspond to the V configuration and the $h = (2, 2, 0)$ representation.

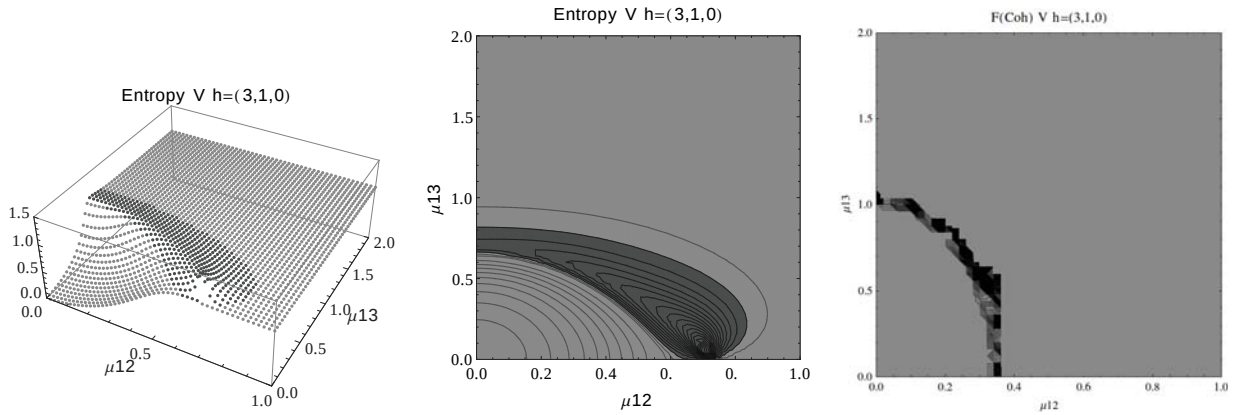

Figure A.31: (**Left**) 3D plot of the entropy of entanglement as a function of the coupling parameters μ_{12} and μ_{13}, the maximum value of the entropy is $S_\varepsilon = 1.4$ and the region where $S_\varepsilon > 1.03$ is shown in dark gray (**Center**) Contour plot of the entropy of entanglement as a function of the coupling parameters μ_{12} and μ_{13}, the region where $S_\varepsilon > 1.03$ is shown in dark gray (**Right**) Fidelity between neighboring coherent states as a function of the coupling parameters μ_{12} and μ_{13}, dark gray region shows the fidelity's minimum (i.e., the phase transition). All figures use $\omega_1 = 1.\bar{3}$, $\omega_2 = 1.\bar{6}$, $\Omega = 0.5$ and correspond to the V configuration and the $h = (3, 1, 0)$ representation.

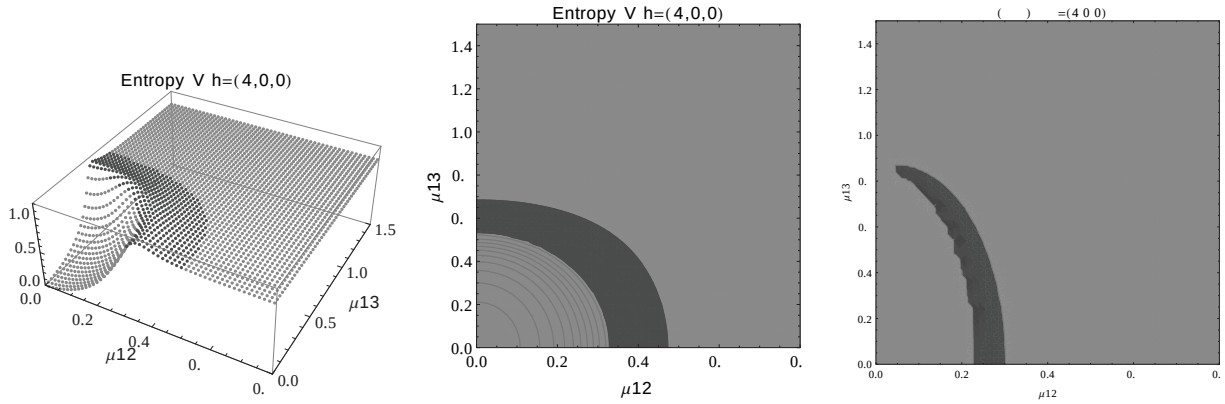

Figure A.32: (**Left**) 3D plot of the entropy of entanglement as a function of the coupling parameters μ_{12} and μ_{13}, the maximum value of the entropy is $S_\varepsilon = 1.15$ and the region where $S_\varepsilon > 1.03$ is shown in dark gray (**Center**) Contour plot of the entropy of entanglement as a function of the coupling parameters μ_{12} and μ_{13}, the region where $S_\varepsilon > 1.03$ is shown in dark gray (**Right**) Fidelity between neighboring coherent states as a function of the coupling parameters μ_{12} and μ_{13}, dark gray region shows the fidelity's minimum (i.e., the phase transition). All figures use $\omega_1 = 1.\bar{3}$, $\omega_2 = 1.\bar{6}$, $\Omega = 0.5$ and correspond to the V configuration and the $h = (4, 0, 0)$ representation.

Bibliography

[1] R. H. Dicke, Phys. Rev. 93, 99 (1954).

[2] K. Hepp and E. H. Lieb, Ann. Phys. 76, 360 (1973).

[3] K. Hepp and E. H. Lieb, Phys. Rev. A 8, 2517 (1973).

[4] Y. K. Wang and F. T. Hioe, Phys. Rev. A 7, 831 (1973).

[5] K. Baumann, C. Guerlin, F. Brennecke and T. Esslinger, Nature (London) 464, 1301 (2010).

[6] D. Nagy, G. Kónya, G. Szirmai and P. Domokos, Phys. Rev. Lett. 104, 130401 (2010).

[7] T. Brandes, Phys. Rep. 408 , 315 (2005).

[8] G. Chen, Z. Chen and J. Liang, Phys. Rev. A 76 , 055803 (2007).

[9] N. Lambert, C. Emary and T. Brandes, Phys. Rev. Lett. 92, 073602 (2004).

[10] N. Lambert, C. Emary and T. Brandes, Phys. Rev. A 71, 053804 (2005).

[11] E. Nahmad-Achar, S. Cordero, O. Castaños and R. López-Peña, Phys. Scr. 90, 074026 (2015).

[12] E. Nahmad-Achar, S. Cordero, R. López-Peña and O. Castaños, J. Phys. A: Math. Theor. 47, 455301 (2014).

[13] S. Cordero, O. Castaños, R. López-Peña and E. Nahmad-Achar, J. Phys. A: Math. Theor. 46, 505302 (2013).

[14] J. Reslen, L. Quiroga and N. F. Johnson, Europhys. Lett. 69, 1 (2005).

[15] P. Zanardi and N. Paunković, Phys. Rev. E 74, 031123 (2006).

[16] H. Goto and K. Ichimura, Phys. Rev. A 77, 053811 (2008).

[17] C. Emary and T. Brandes, Phys. Rev. E 67, 066203 (2003).

[18] C. Emary and T. Brandes, Phys. Rev. Lett. 90, 044101 (2003).

[19] E. Romera, R. del Real and M. Calixto, Phys. Rev. A 85, 053831 (2012).

[20] E. Romera, M. Calixto and Á. Nagy, Europhys. Lett. 97, 20011 (2012).

[21] O. Castaños, R. López-Peña, E. Nahmad-Achar, J. G. Hirsch, E. López-Moreno and J. E. Vitela, Phys. Scr. 79, 065405 (2009).

[22] O. Castaños, E. Nahmad-Achar, R. López-Peña and J. G. Hirsch, Phys. Scr. 80, 055401 (2009).

[23] O. Castaños, E. Nahmad-Achar, R. López-Peña, and J. G. Hirsch, Phys. Rev. A 83, 051601 (2011).

[24] O. Castaños, E. Nahmad-Achar, R. López-Peña, and J. G. Hirsch, Phys. Rev. A 84, 013819 (2011).

[25] O. Castaños, E. Nahmad-Achar, R. López-Peña, and J. G. Hirsch, Phys. Rev. A 86, 023814 (2012).

[26] J. G. Hirsch, O. Castaños, E. Nahmad-Achar and R. López-Peña, Phys. Scr. 2013, 014033 (2013).

[27] H.I. Yoo and J.H. Eberly, *Phys. Rep. 118, 239 (1985)*.

[28] O. Civitarese and M. Reboiro, Phys. Lett. A 357, 224 (2006).

[29] N.H. Abdel-Wahab, Phys. Scr. 76, 244 (2007).

[30] N.H. Abdel-Wahab, *Mod. Phys. Lett. B 22, 2587 (2008)*.

[31] M Hayn, C. Emary and T. Brandes, Phys. Rev. A 84, 053856 (2011).

[32] M. Hayn, C. Emary and T. Brandes, Phys. Rev. A 86, 063822 (2012).

[33] S. Cordero, R. López-Peña, O. Castaños and E. Nahmad-Achar, Phys. Rev. A 87, 023805 (2013).

[34] S. Cordero, E. Nahmad-Achar, R. López-Peña and O. Castaños, Phys. Rev. A 92, 053843 (2015).

[35] S. Cordero, O. Castaños, R. López-Peña and E. Nahmad-Achar, Phys. Rev. A 94, 013802 (2016).

[36] V.N. Chernega, O.V. Manko and V.I. Manko, J. Russ. Laser Res. 38, 416 (2017).

[37] A.E. Kozhekin, K. Mølmer and E. Polzik, Phys. Rev. A 62, 033809 (2000).

[38] A. Gorshkov, A. André, M. Fleischhauer, A. Sørensen and M. Lukin, Phys. Rev. Lett. 98, 123601 (2007).

[39] J. Nunn, I.A. Walmsley, M.G. Raymer, K. Surmacz, F.C. Waldermann, Z. Wang and D. Jaksch Phys. Rev. A 75, 011401 (2007).

[40] J.L. Morton, A.M. Tyryshkin, R.M. Brown, S. Shankar, B.W. Lovett, A. Ardavan, T. Schenkel, E.E. Haller, J.W. Ager, and S.A. Lyon, *Nature 455, 1085 (2008)*.

[41] I.M. Gelfand and M.L. Tsetlin, Dokl. Akad. Nauk 71, 825 (1950).

[42] A. Arne, M. Kalus, A. Huckleberry and J.V. Delft, J. Math. Phys. 52, 023507 (2011).

[43] R. López-Peña, S. Cordero, E. Nahmad-Achar and O. Castaños, Phys. Scr. 90, 068016 (2015).

[44] M. Calixto, E. Romera and R. del Real, J. Phys. A 45, 365301 (2012).

[45] Chernega, V.N.; Man'ko, O.V.; Man'ko, V.I. Triangle Geometry for Qutrit States in the Probability Representation. *J. Russ. Laser Res.* **2017**, *38*, 416–425.

[46] Chernega, V.N.; Man'ko, O.V.; Man'ko, V.I. Deformed entropy and information relations for composite and noncomposite systems. *Found. Phys.* **2015**, *45*, 783–789.

[47] L.F. Quezada and E. Nahmad-Achar, Phys. Rev. A 95, 013849 (2017).

[48] L.F. Quezada and E. Nahmad-Achar, Entropy 20, 72 (2018).